University of Alberta

Cathode Materials Development for Proton Conducting SOFCs

by

Guihua Zhou

A thesis submitted to the Faculty of Graduate Studies and Research
in partial fulfillment of the requirements for the degree of

Master of Science
in
Chemical Engineering

Department of Chemical and Materials Engineering

Abstract

Thin film electrolyte and new cathode catalysts were developed to improve the performance of proton conducting solid oxide fuel cells (SOFCs).

Electrolyte $BaCe_{0.7}Zr_{0.1}Y_{0.2}O_{3-\delta}$ (BCZY) and cathode materials $La_{0.6}Sr_{0.4}Co_{0.2}Fe_{0.8}O_{3-\delta}$ (LSCF) and $Sr_{0.7}Ce_{0.3}MnO_{3-\delta}$ (SCM) were synthesized using the citrate-nitrate combustion method, and characterized using XRD. Thin film electrolyte was successfully prepared using a spin coating technique.

Two cathode catalysts were developed: a composite cathode comprising Ag-modified LSCF+BCZY, and SCM. Chemical compatibility between LSCF and BCZY and chemical stability of LSCF in CO_2-containing atmosphere were demonstrated. The electrochemical performance of the composite cathode was dependent on Ag content in the composite cathode, peaking at a power density of 563 mW.cm^{-2} at 700 °C for Ni+BCZY|BCZY|10 wt% Ag-(LSCF+BCZY) thin film button cell. The performance of SCM was dependent on the cathode firing temperature. The highest peak power density, 378 mW.cm^{-2}, was obtained at 700 °C for Ni+BCZY|BCZY|SCM single cell with SCM fired at 1100 °C.

Acknowledgements

Table of Contents

List of Figures

List of Abbreviations

AFCs	Alkaline fuel cells
ASR	Area-specific resistance
BCZY	$BaCe_{0.7}Zr_{0.1}Y_{0.2}O_{3-\delta}$
BCY	Y-doped $BaCeO_3$
EIS	Electrochemical impedance spectroscopy
GDC	Gadolinia doped Ceria
LSCF	$La_{0.6}Sr_{0.4}Co_{0.2}Fe_{0.8}O_{3-\delta}$
LSF	strontium doped lanthanum ferrite
LSGM	Lanthanum strontium gallate magnesite
LSM	$La_{1-x}Sr_xMnO_{3-\delta}$
MCFCs	Molten carbonate fuel cells
MEA	Membrane electrode assemblies
MIEC	Mixed ionic and electronic conductors
OCV	Open circuit voltage
PAFCs	Phosphoric acid fuel cells
PEMFCs	Polymer electrolyte membrane fuel cells
SCM	$Sr_{0.7}Ce_{0.3}MnO_{3-\delta}$
SEM	Scanning Electronic Microscope
SOFCs	Solid oxide fuel cells
TEC	Thermal expansion coefficient
TGA	Thermogravimetric analysis

TPB	Tripe-phase boundary
XRD	X-ray diffraction
YSZ	Yttria stabilized zirconia

Chapter 1   Introduction

1.1 Energy Demand and CO$_2$ Emissions

Global economic growth and the rise in standards of living around the world result in considerable demand growth on energy resources. Figure 1.1 shows the world marketed energy consumption through 2035 projected by International Energy Administration *(1)*. It is clear that fossil fuels, i.e., liquid fuels, coal and natural gas, still account for the majority of current power generation and are projected to continue supplying much of the energy used worldwide for the foreseeable future.
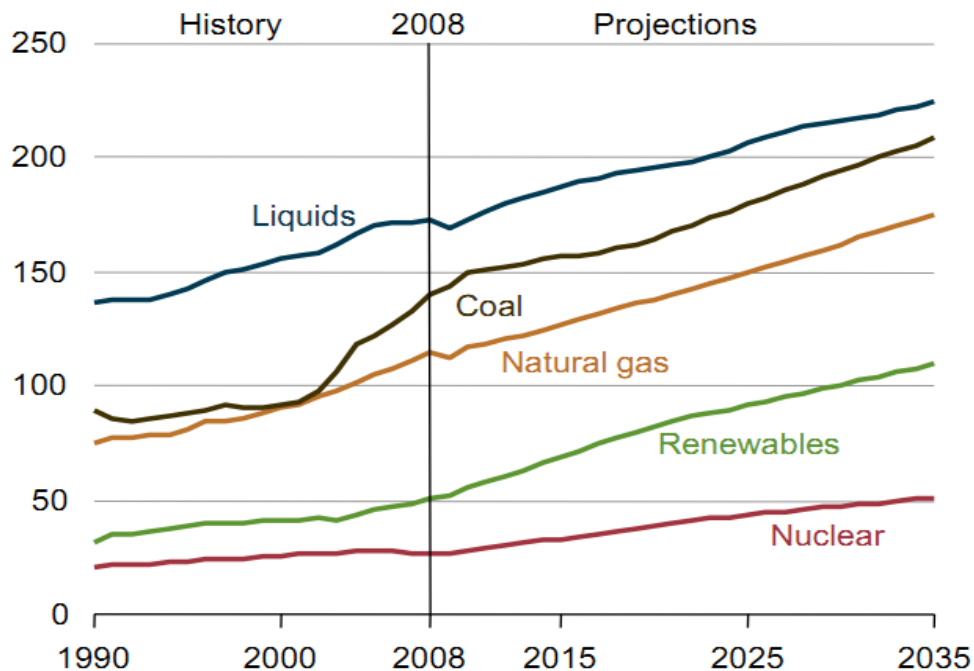
Figure 1.1. World marketed energy consumption by fuel type (quadrillion Btu) *(1)*.

The problems with direct usage of fossil fuels are well known. They are not only non-renewable but also cause environmental problems with emission of the greenhouse gas, CO_2. As shown in Figure 1.2 *(1)*, worldwide energy-related CO_2 emissions from the burning of carbonaceous fuels which include liquid fuels, natural gas, and coal all are increasing.
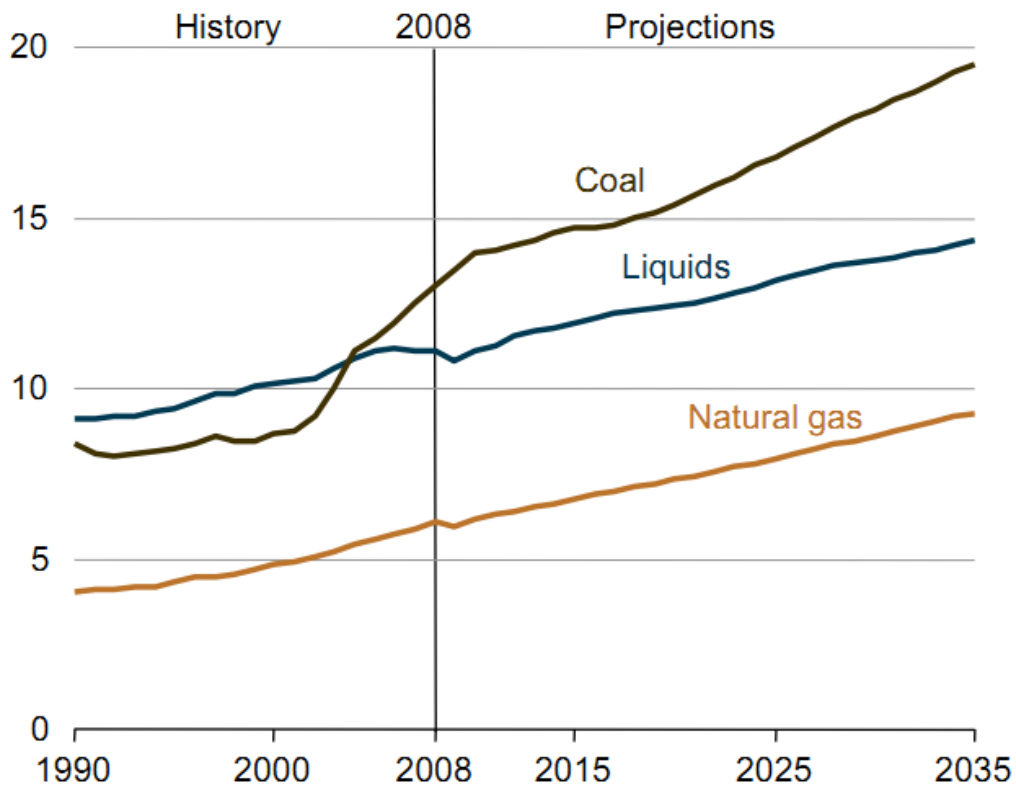
Figure 1.2. World energy-related CO_2 emissions by fuel type (billion metric tons) *(1)*.

Elevated CO_2 concentration in the atmosphere results in additional absorption and emission of thermal infrared radiation in the atmosphere and

produces net warming of the earth. The global surface temperature has been increasing rapidly in the last few decades shown in Figure 1.3 *(2)*. According to the latest Assessment Report from the Intergovernmental Panel on Climate Change, "most of the observed increase in globally averaged temperatures since the mid-20th century is very likely due to the observed increase in anthropogenic greenhouse gas concentrations" *(2)*.
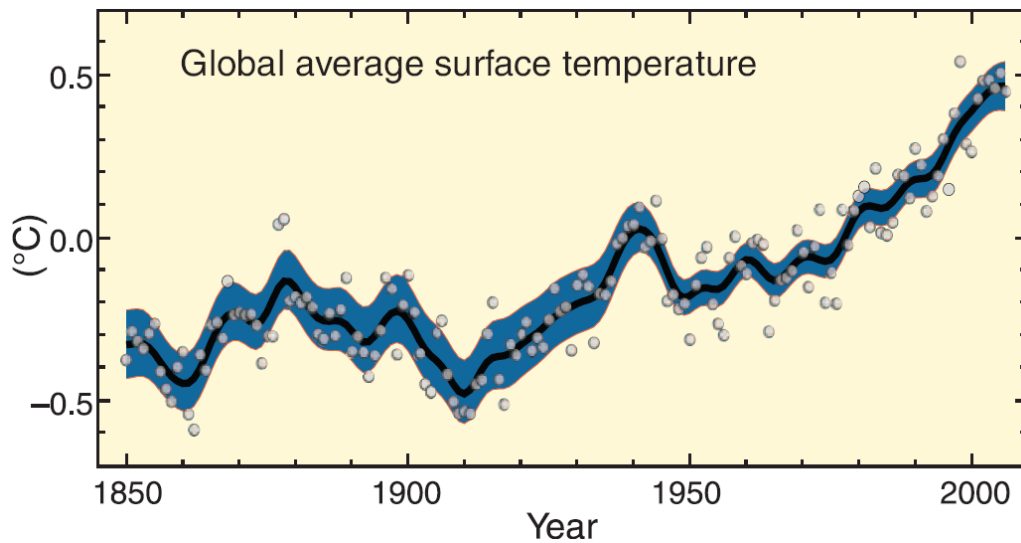
Figure 1.3. Observed changes in global average surface temperature relative to corresponding averages for the period 1961-1990 *(2)*.

As the increasing demand of energy has to be satisfied to maintain present living standards, several nations are gradually switching their attention to renewable energies and to use of the limited non-renewable resources in a more efficient way. Interestingly, renewable energy is the world's fastest growing form of energy, and the renewable share of total energy use is projected to

increase from 10% in 2008 to 14% in 2035 *(1)*. Fuel cells are one of the potential efficient technologies which many researchers have been working on for energy generation.

1.2 Fuel Cells

The phenomena now used in fuel cells were observed, described and explained by William Grove in 1839. There was no large scale investigation until that at Cambridge in the 1950's because the most suitable materials were not readily available, and there was no significant motivation. In recent years, fuel cells have been attracting researchers' attention and considered as one of the alternative methods for future power generation and chemical conversions due to their intriguing advantages *(3, 4)*.

Firstly, they are potentially more fuel efficient than combustion engines because they produce electricity directly from chemical energy stored in the fuel while the efficiency of combustion engines is limited by the laws of thermodynamics, i.e., Carnot cycle thermodynamics. Secondly, they are almost silent, as the cell itself has no moving parts. Thirdly, fuel cells can dramatically decrease regulated pollutant emissions by several orders of magnitude, for example NO_x and CO_2 emissions are reduced by at least 20% compared to the base-case of an equivalent internal combustion engine vehicle when hydrocarbon gas is used as fuel *(5)*.

Basically there are five types of fuel cells as illustrated in Figure 1.4 *(6)*. SOFCs employ a solid ceramic membrane as the electrolyte and operate

typically at the temperatures between 500 °C and 1000 °C. SOFCs have high fuel flexibility with non-precious metal as catalyst, but the high operating temperature can cause sealing issues and the need for expensive components and fabrication. Molten carbonate fuel cells (MCFCs) employ a molten mixture of alkali carbonates, for example, Li_2CO_3 and K_2CO_3 immobilized in a $LiAlO_2$ matrix, as electrolyte with carbonate ion, CO_3^{2-} as the mobile charge carrier and operate at about 650 °C. The issues with MCFCs include the need for CO_2 recycling and that the electrolyte is molten and corrosive. Also, MCFCs use Pt as catalyst that is susceptible to CO and S poisoning. Phosphoric acid fuel cells (PAFCs), as the name indicates, employ liquid H_3PO_4 trapped in a thin SiC matrix as electrolyte and operate around 200 °C. Polymer electrolyte membrane fuel cells (PEMFCs) employ a proton conducting polymer, usually a perfluorinated sulfonic acid polymer as electrolyte and the operating temperature is limited to 90 °C at atmospheric pressure, mostly 80 °C. A low operating temperature provides good start-stop capabilities and makes a cell suitable for portable applications but PEMFCs typically use Pt as catalyst, and the poor CO and S tolerance of Pt requires expensive, highly purified fuel. Alkaline fuel cells (AFCs) employ aqueous potassium hydroxide as electrolyte and operate at 70°C. AFCs can use non-precious metal as catalysts but have to use the H_2-O_2 system.
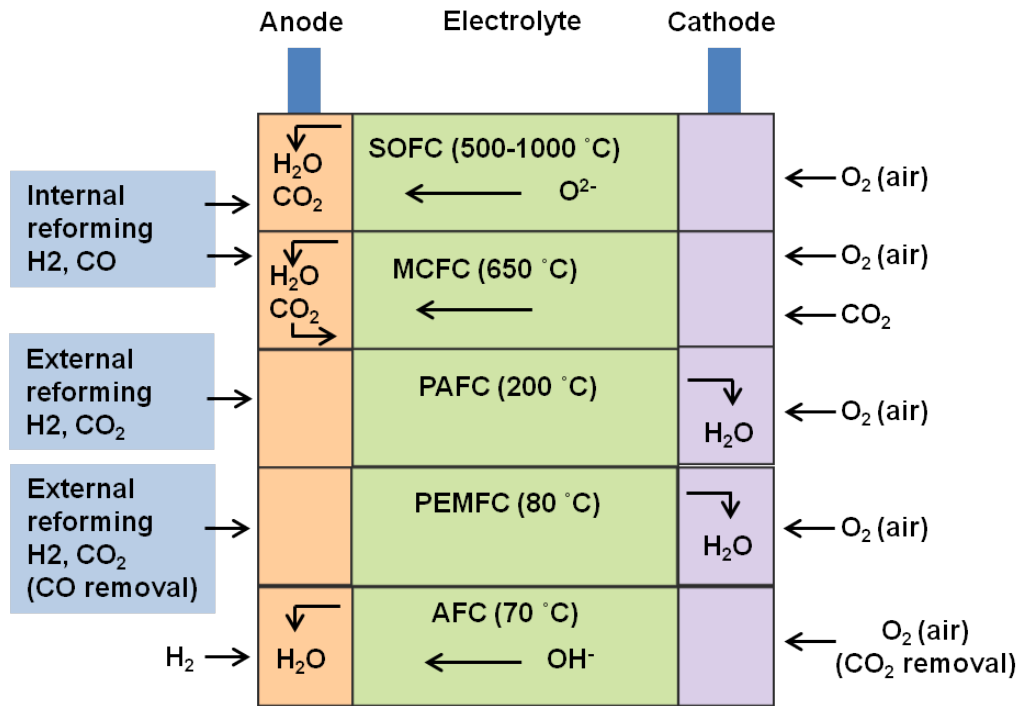
Figure 1.4. Schematic illustration of fuel cells by type *(6)*.

Among these five types of fuel cells, SOFCs are the most promising energy technology in development in terms of power density. Firstly, the elevated temperature of operation of SOFC gives them the potential to operate with a wide range of fuels, which include carbon-containing gases such as hydrocarbons, syngas and even H_2S-containing gases *(7-10)*. Secondly, operation at high temperature also allows the use of relatively inexpensive ceramic materials as electrolyte, and electrodes other than precious metals such as Pt or Pd required for operation of lower temperature systems. Besides, SOFCs are able to employ cogeneration schemes utilizing the high quality heat generated. The electrical efficiency of SOFCs to date typically is about 50-60%,

the highest among all the fuel cells. When the electrical power is combined with generated heat, the efficiency can reach 90% *(3)*.

A typical SOFC uses yttria stabilized zirconia (YSZ) as electrolyte through which the oxide ions produced at the cathode are transported to the anode. The transport process is thermally activated and usually requires an operating temperature above 700 °C for useful systems. Therefore, basically, SOFCs with YSZ as electrolyte usually work at temperatures in the range 800-1000 °C as a consequence of needing to overcome the activation energy for ion migration in the solid ceramics. In spite of the advantages with the high operating temperature as mentioned before, high temperature operation poses challenges. One consequence of high temperature operation is a slow start-up. The high temperature also imposes stringent requirements on the SOFC components. The component materials have to possess high durability under start-stop cycling to avoid expansion-contraction and high temperature corrosion or oxidation issues. It is desirable to decrease the operating temperature of SOFCs so that much less expensive materials may be used *(6)*. Proton conducting SOFCs potentially meet the low temperature needs which mostly operate at intermediate temperatures (500-700°C) as proton conduction is sufficient at lower temperatures than oxide ion conduction.

1.3 Proton Conducting SOFCs

Compared with SOFCs based on oxide ion conductors, SOFCs based on proton conductors offer several advantages *(11-14)*. Importantly, proton

conducting SOFCs can operate at intermediate temperature (500-700 °C) partially due to lower activation energy for proton than for oxide ion migration, and that makes it easier to find suitable connection and sealing materials. Additionally, the fuel will not be diluted during fuel cell operation since water vapour is produced in the cathode compartment where it is swept away by air, not in the anode compartment as it is for an oxide ion conducting SOFC.

1.3.1 Challenges

Although use of proton conductor as electrolyte reduces the operating temperature of a SOFC, the performances of many of these cells are still less than adequate for practical applications *(15)*, primarily due to the lack of proper cathode materials that are both highly active and compatible with the electrolytes *(16)*. Up to now, the cathode materials employed in protonic SOFCs are primarily the well-studied mixed oxide ionic and electronic conductor for oxide ion conducting SOFCs, for example, $La_xSr_{1-x}Co_yFe_{1-y}O_{3-\delta}$ *(17)* and $Sm_{0.5}Sr_{0.5}CoO_3$ (SSC) *(16)*. However, the electrode reaction mechanism has not been investigated sufficiently and issues such as chemical incompatibility between cathode and electrolyte material still exist. For example, SSC, reported as a cathode for protonic SOFC, is highly reactive with the electrolyte material BCZY *(16)*.

1.3.2 Objectives

The primary goal of this project is to investigate the potential application of proton conducting SOFCs with H_2 as fuel by developing new cathode

materials. Commonly used electrolyte BCZY and anode catalyst nickel are employed in the system, so that the performance of different cathodes can be compared. Developments of thin film electrolyte and cathode materials are two methods used here to improve the performance of protonic SOFCs. The targeted requirements for a thin film electrolyte are high density to prevent gas crossover and small thickness with low ohmic loss. The targeting requirements for suitable cathode materials are: high electro-catalytic activity, chemically inert to reactions with other components, electronically conductive, and chemically stable in the humid air cathode compartment atmosphere.

This thesis comprises an overview of fuel cell background theory, and describes the experimental method, results and discussion, and conclusions.

Chapter 2 Theory and Literature Review

2.1 Principles of SOFCs

Solid oxide fuel cells include an electrolyte, cathode and anode, as shown in Figure 2.1, with appropriate interconnects between cells, and current collectors connecting the cells electronically with the external circuit.

$$H_2 \rightarrow 2H^+ + 2e^-$$

$$2H^+ + \frac{1}{2}O_2 + 2e^- \rightarrow H_2O$$
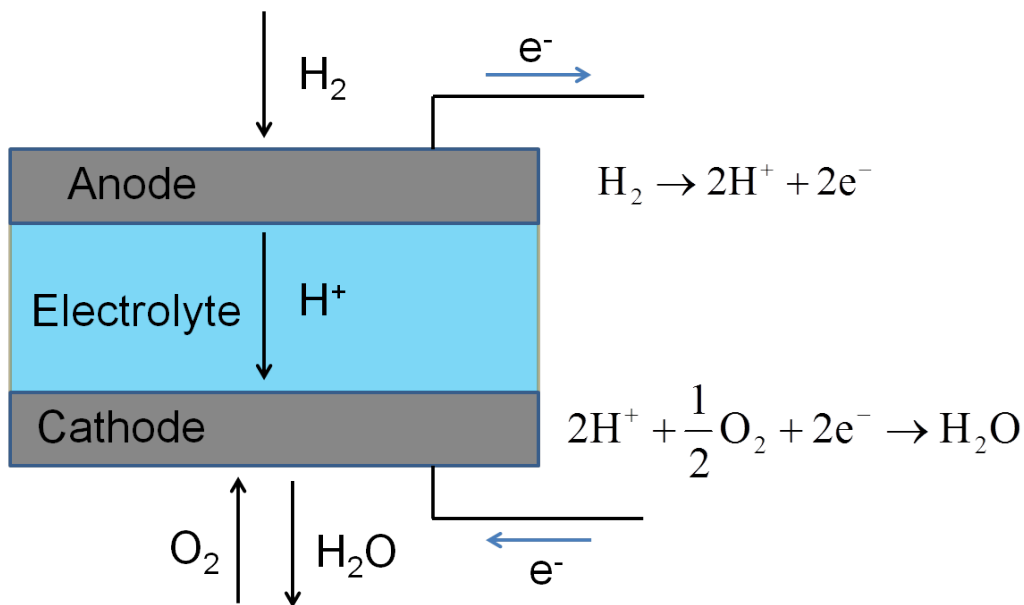
Figure 2.1. Schematic illustration of a proton conducting SOFC.

Figure 2.1 illustrates schematically a reaction mechanism in a proton conducting SOFC. Gaseous fuels are fed continuously to the anode side where they form protons which react with lattice oxygen of the electrolyte structure to form hydroxide intermediate species. The protons are then transferred to neighboring oxygen and so migrate through the electrolyte to the cathode side.

Water is produced at the cathode side as the protons react with oxygen from the oxidant. The electrochemical reactions shown in Figure 2.1 take place at the intersection area among electrolyte, gas phase and electrode, also known as triple phase boundary (TPB), to produce an electrical current.

The performance of a fuel cell can be elucidated with a current-voltage (*I-V*) curve which shows the variation of voltage output from the fuel cell with given current output curve, as illustrated in Figure 2.2.
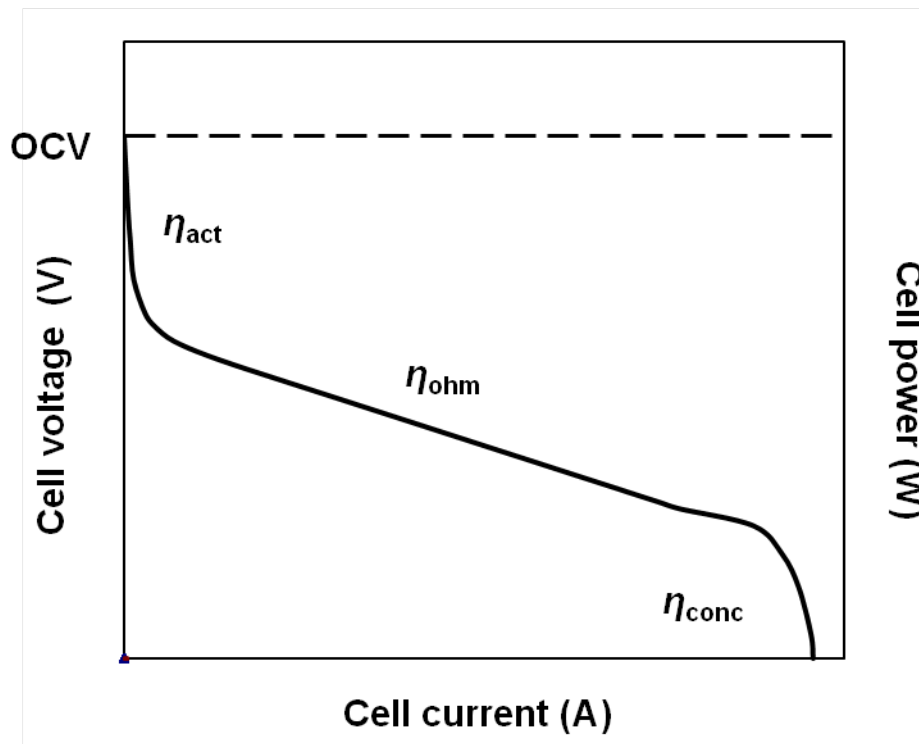
Figure 2.2. Fuel cell *I-V* curve.

The actual voltage output is the thermodynamically predicated voltage reduced by the voltage drops due to various losses and can be expressed using Equation 2-1:

$$V = E_{\text{thermo}} - \eta_{\text{act}} - \eta_{\text{ohm}} - \eta_{\text{conc}} \tag{2-1}$$

where V = the operating potential

E_{thermo} = thermodynamically predicted voltage

η_{act} = activation loss due to reaction kinetics

η_{ohm} = ohmic loss from ionic and electronic resistance

η_{conc} = concentration loss due to mass transport

2.1.1 Thermodynamically Predicted Voltage

In SOFCs, electrons do useful work as electricity is produced when they flow from anode to cathode side through an external circuit. The Gibbs free energy (ΔG) of reaction is directly related to the potential available from the reaction *(18)*.

$$\Delta G = -nFE \tag{2-2}$$

where n = number of electrons, F = Faraday's constant, and E is the reversible voltage. The reversible voltage generated by SOFC under standard-state is thus:

$$E^0 = -\frac{\Delta G^0}{nF} \tag{2-3}$$

The predicted reversible voltage under non-standard-state conditions is affected by several factors: chemical activity of reactants and products, and temperature, as expressed by the Nernst equation *(3)*:

$$E = E_T - \frac{RT}{nF} \ln \frac{\Pi a_{product}^{v_i}}{\Pi a_{reactant}^{v_i}} \tag{2-4}$$

where E_T is reversible voltage at temperature T, R is the gas constant, $a_{product}$ is the activity of products, $a_{reactant}$ is the activity of reactants and v_i is the corresponding stoichiometric coefficient of each species.

2.1.2 Activation Polarization

Activation polarization due to electrochemical reaction is the dominant cause of potential loss at the initial part of the curve. In this range, electronic barriers for the reaction have to be overcome prior to electron and ion flow.

2.1.3 Ohmic Loss

Ohmic loss is due to resistance to charge transport when charges flow through the electrolyte and electrodes. As resistance remains constant for a specific material, ohmic loss increases over the whole range of current according to Ohm's law (3):

$$\eta_{Ohm} = IR_{total} \tag{2-6}$$

where I is current and R_{total} is total resistance due to charge transport. Use of a thin film electrolyte and high-conductivity materials can decrease resistance and so reduce ohmic loss. With this in mind, development of thin film SOFCs and highly conductive materials are two important strategies in SOFC research.

2.1.4 Concentration Polarization

Concentration loss is caused by mass transport limitations at high current density. The main transport processes are diffusion of both feeds and products in the bulk, and molecular diffusion within the electrodes. Concentration differences in the catalyst layer can affect fuel cell performance by reducing thermodynamic voltage and reaction rate (3).

$$\eta_{conc} = c \ln \frac{j_L}{j_{L-j}} \tag{2-7}$$

where c is a constant, j is current density and j_L is the limiting current density when the reactant concentration in the catalyst layer drops close to zero. Concentration loss can be minimized by optimization of mass transport in the flow structures and electrodes.

2.2 Cathodic Reaction in SOFCs

The cathode is a component of a SOFC at which the oxidant, typically oxygen, is reduced.

2.2.1 Cathode Processes for Oxide Ion Conducting SOFCs

For oxide ion conducting SOFCs, the following electrochemical reaction takes place (19):

$$O_2 + 2V_O^{\cdot\cdot} + 4e' = 2O_O^x \tag{2-8}$$

where, in Kröger-Vink notation (20), $V_O^{\cdot\cdot}$ is a vacant oxygen site, and O_O^x is an oxide ion at a regular oxygen site. The equation illustrates that oxygen reduction requires the presence of molecular oxygen, electrons and the means

for oxide ions to be transported away from the reaction sites into the bulk of the electrolyte.

The reduction reaction mechanisms are illustrated schematically in Figure 2.3 (21). The behaviour of cathodes possessing only electronic conductivity, such as $La_{1-x}Sr_xMnO_{3-\delta}$ (LSM), is illustrated in Figure 2.3 (a). Oxygen diffuses into the pore space, dissociates and then moves to the TPB. The oxide ions produced at the TPB are transferred into the bulk of the electrolyte.
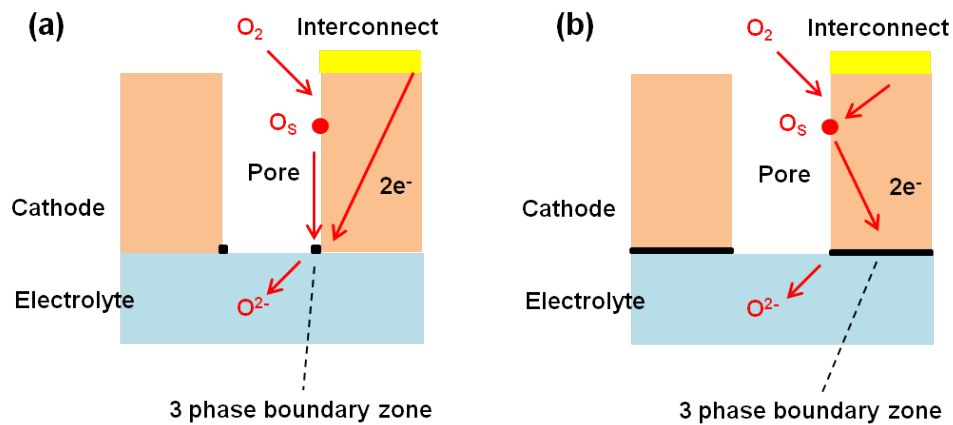
Figure 2.3. Schematic representation of cathode structure with (a) poor, and (b) good ionic conductor (21).

For a mixed conducting cathode, such as $La_{1-x}Sr_xCo_yFe_{1-y}O_3O_{3-\delta}$, as shown in Figure 2.3 (b), the reaction sites are extended to the electrode surface from the electrode/electrolyte interface. Oxygen molecules diffuse first into the porous structure, then are reduced to ions at the surface of the mixed conducting cathode material, at the TPB between cathode, electrolyte and gas

phase, and also at the intersection between cathode material and gas phase. The generated oxide ions then diffuse through the cathode material to the electrolyte. Due to the larger area available for reaction and ion transfer across the interface, the mixed conducting cathodes are expected to have lower resistance.

2.2.2 Cathode Processes for Proton Conducting SOFCs

For proton conducting SOFCs, the cathode reaction mechanism is different from that for oxide ion conducting SOFCs as protons are involved in the process besides oxygen species. The reduction can be described with the following equation:

$$O_2 + 4OH_O^\cdot + 4e' \rightarrow 2H_2O + 4O_o^x \tag{2-9}$$
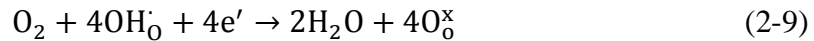
Besides the molecular oxygen and electrons required for oxide ion conducting SOFCs, a means by which protons are transported from the electrolyte into the reaction sites is a necessity for the reduction reaction of proton conducting SOFCs.

Figure 2.4 *(22)* schematically illustrates the four different reduction processes based on cathode materials: pure electronic conductors, mixed oxide ionic and electronic conductors, composite conductors composed of a protonic conductor and an electronic conductor , and composite conductors composed of a protonic conductor and an oxide ionic and electronic mixed conductor. With an electronic conductor, such as LSM as cathode catalyst, as demonstrated in Figure 2.4 (a), the reaction sites are limited to the TPB. The dissociated oxide ions have to transfer along the surface of the cathode phases to reach a TPB to

react with protons and produce water. With mixed ionic and electronic conductors as cathode materials, such as $La_xSr_{1-x}Co_yFe_{1-y}O_{3-\delta}$ shown in Figure 2.4 (b), the reaction sites are also limited to TPB as in case (a), but the transfer paths of oxygen species to TPB are greatly enlarged as the dissociated oxide ions can transfer through the bulk as well as along the surface of the cathode. With composite conductors composed of a protonic conductor and an electronic conductor as cathode materials, Figure 2.4 (c), the reacting sites are greatly enlarged beyond TPB to the bulk of the cathode where the protonic and ionic conductors meet. For the last case shown in Figure 2.4 (d), besides the enlarged TPB, the transfer paths of oxygen species to reaction sites are also enlarged and it is the best cathode among the four types. Therefore, we want our cathode to be the last type, which is a composite cathode comprising both a protonic conductor (mostly of the same material as the electrolyte) and a mixed conductor.
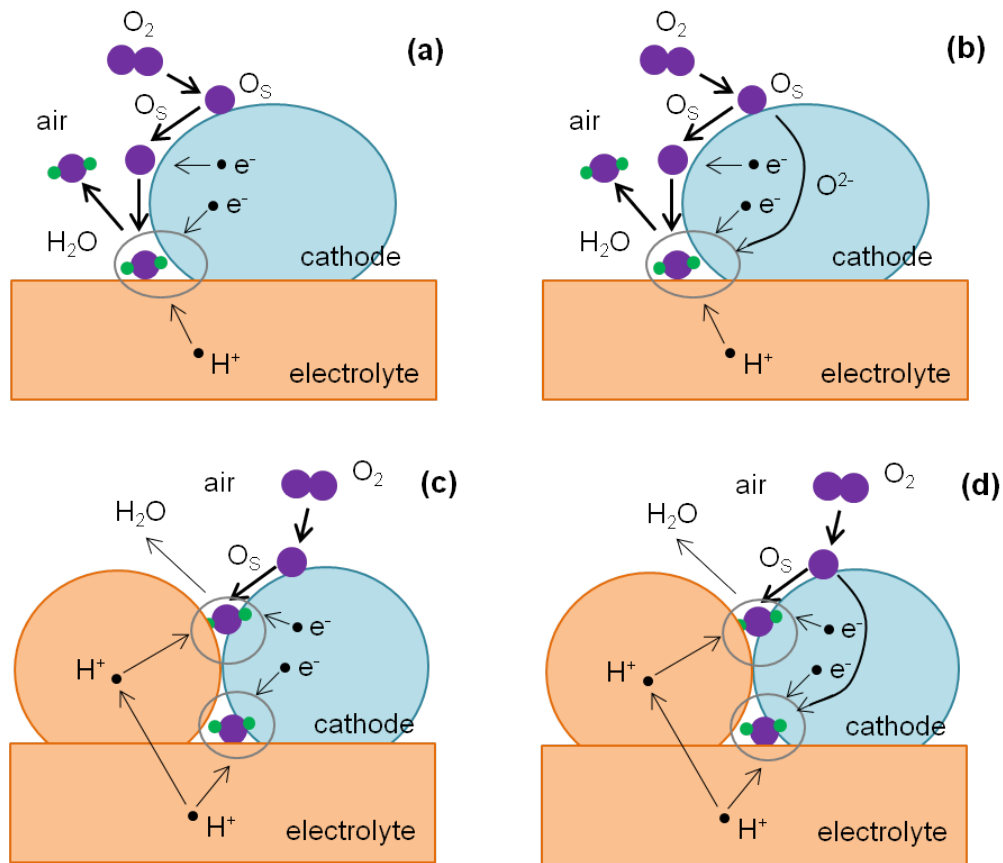
Figure 2.4. A schematic representation of the cathode reaction mechanisms for a proton conducting SOFC with (a) electronic conductor; (b) mixed oxide ionic and electronic conductor; (c) composite composed of a proton conductor and an electron conductor; and (d) composite composed of a proton conductor and a mixed oxide ionic and electronic conductor, as cathode materials *(22)*.

2.3 Development of Cathode Materials

The cathode materials primarily investigated to date for use in SOFCs are oxides such as ABO_3 perovskite oxides, oxides having K_2NiF_4 structures and $AA'B_2O_{5+\delta}$ double perovskite oxides among which ABO_3 perovskite oxides remain the most widely used due to its development maturity and structure simplicity *(21)*.

2.3.1 ABO_3 Perovskite Oxides

The unit cell of the ABO_3 perovskite structure is shown in Figure 2.5 *(23)*. Oxide anions form a lattice with A and B cations having different sizes. The A cations are larger than the B cations. The ideal cubic-symmetry structure has the B cation in 6-fold coordination, surrounded by an octahedron of anions, and the A cation in 12-fold cuboctahedral coordination.
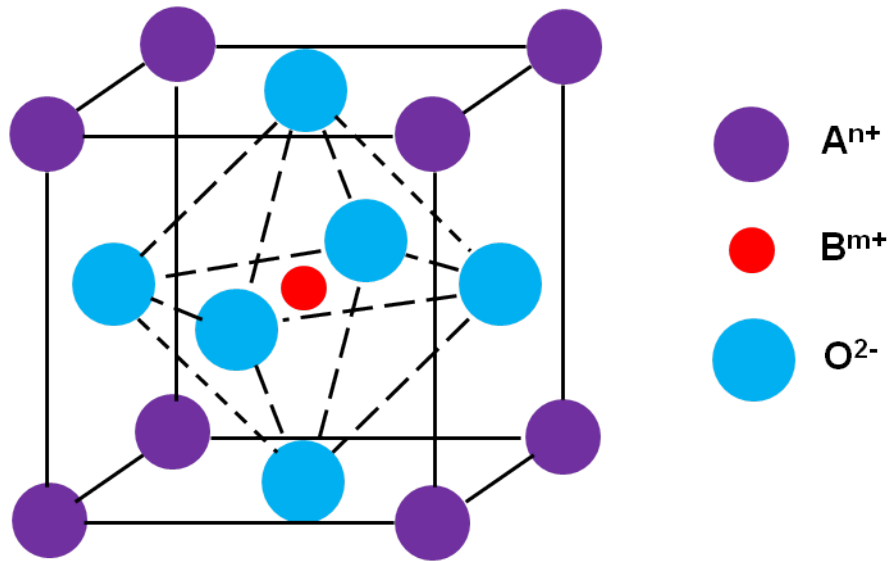
Figure 2.5. The unit cell of perovskite structure *(23)*.

Considerable research has been conducted into use of perovskite oxides as cathode materials for use with each of YSZ, gadolinia doped ceria (GDC) and lanthanum strontium gallate magnesite (LSGM) as the electrolyte. Among these cathode materials, lanthanum manganite-based perovskites and lanthanum cobaltite and ferrite perovskites have been investigated extensively and proved to be practical choices for use as cathodes *(24)*.

1. Lanthanum Manganite-based Perovskites

LSM is the most widely studied cathode material among the lanthanum manganite family. It has high electrical conductivity, high thermal stability, and chemical compatibility with YSZ, GDC, and LSGM at electrochemical cell operating conditions. However, its oxide ionic conductivity is very low and thus limits the rate of the oxygen reduction reaction. Three steps can be identified for reduction of O_2 on LSM: surface dissociative adsorption and diffusion,

charge transfer, and oxide ion migration into the zirconia electrolyte phase *(25)*. The rate of reaction is determined by the dissociative adsorption and diffusion at the LSM electrode surface at low temperatures and the oxide ion migration/diffusion into the electrolyte at high temperatures *(25)*.

Mizusaki et al. showed that electronic conductivity of $La_{1-x}Sr_xMnO_{3+\delta}$ ($0 \leq x \leq 0.7$) increased with the value of x and reached a peak at x = 0.5 *(26)*. The conductivity (σ) also depends on the partial pressure of oxygen. In the oxygen excess region, i.e., $P_{O_2} > 10^{-5}$ bar, σ is constant. In the oxygen deficient region, conductivity increases with oxygen concentration *(26)*. Endo et al. showed that the oxide ionic conductivity of LSM was as small as $5.9*10^{-8}$ S.cm^{-1} at 800 °C *(27)*. Thermal expansion coefficient (TEC) of undoped $LaMnO_3$ is $11.33*10^{-6}$ K^{-1} *(28)*, which is slightly higher than that of YSZ, about $10.3*10^{-6}$ K^{-1} in the range between 50 °C to 1000 °C *(24)*.

The oxygen surface exchange coefficient (k_O) and oxygen self-diffusion coefficient (D_O) are used to characterize the oxygen diffusion and transport properties for the oxygen reduction reaction at the electrode/electrolyte interface *(24, 29)* and materials with high value of k_O and D_O have good oxygen surface and bulk transport properties. Carter et al. studied the oxygen diffusion coefficient and oxygen surface exchange coefficient of LSM *(29)*. At 900 °C, D_O is of the order of 10^{-14}-10^{-12} cm^2.s^{-1} and k_O is of the order of 10^{-8} cm.s^{-1} *(29)*. At 1000 °C, D_O for $La_{1-x}Sr_xMnO_{3-\delta}$ (x = 0.05, 0.10, 0.15 and 0.20) is of the order of 10^{-12}-10^{-11} cm^2.s^{-1} and oxide ionic conductivity is estimated to be 10^{-7} to 10^{-6} S.cm^{-1} *(30)*.

The electrochemical activities of these materials are low when used in SOFC due to the limited reaction sites available on the surfaces of LSM cathodes. The polarization resistivity for the reduction of O_2 is 0.39 $\Omega.cm^2$ at 900 °C and increases to 55.7 $\Omega.cm^2$ at 700 °C *(31)*. Researchers have developed different ways to improve the electro-catalytic activities of the LSM cathodes. Among them, development of composite cathodes with proper composition and optimization of electrode structure are common strategies *(32-35)*.

2. Lanthanum Cobaltite and Ferrite Perovskites

LSM shows good performance at high temperature, but it is not suitable for use at temperatures below 800 °C due to its low ionic conductivity *(24)*. Therefore, development of cathode materials capable of operating at intermediate temperature is required. Unlike LSM, doped lanthanum ferrite and lanthanum cobaltite are mixed ionic and electronic conductors (MIEC).

A-site strontium doped lanthanum ferrite (LSF) perovskites have compatible TEC with many electrolytes *(36-38)*. A chemical compatibility study between LSF and YSZ showed no reaction occurred up to 1400 °C. Coffey et al. found that LSF doped at the B site with aluminum *(39)* or nickel *(40)* were not as active as undoped LSF.

Cobalt-containing perovskites show high electronic and ionic conductivities and good electrochemical activity for oxygen reduction. The electronic conductivity of $La_{1-x}Sr_xCoO_3$ is of the order of 10^2 -10^3 $S.cm^{-1}$ and reaches a maximum value at x = 0.4 *(41, 42)*. Teraoka et al. measured oxide

ionic conductivities of $La_{0.6}Sr_{0.4}Co_{0.8}Fe_{0.2}O_{3-\delta}$ and $La_{0.8}Sr_{0.2}CoO_{3-\delta}$ to be 0.18 and 1.2 S.cm^{-1} at 900 °C, respectively (43).

Lanthanum cobalt-based perovskites have high oxygen diffusion and exchange rate. Carter et al. reported D_O of the order of 10^{-8} cm^2.s^{-1}, 4-6 orders of magnitude higher than that of LSM while k_O was reported to be of the order of 10^{-6} cm.s^{-1} in the temperature range 700-900 °C for $La_{0.5}Sr_{0.5}CoO_{3-\delta}$ (29). Unfortunately, lanthanum and cobalt-based perovskites have high TEC. According to Petric et al., the TEC of $La_{1-x}Sr_xCoO_{3-\delta}$ increases from $18.5*10^{-6}$ K^{-1} to $26.0*10^{-6}$ K^{-1} as x increases from 0.1 to 0.9 (42). In addition, cobalt-based oxides are chemically unstable under reducing atmospheres (44).

$La_xSr_{1-x}Co_yFe_{1-y}O_{3-\delta}$ offers good electronic and ionic conductivity (45, 46), high oxygen diffusion and exchange rate (29), and excellent catalytic activity (47). $La_{0.6}Sr_{0.4}Co_{0.2}Fe_{0.8}O_{3-\delta}$ shows good compromise between conductivity and TEC. Petric et al. determined its conductivity of 333 S.cm^{-1} and TEC of $17.5*10^{-6}$ K^{-1} at 800 °C (42).

The good performance of LSCF has generated much interest and the system has been studied by several groups. Addition of the electrolyte phase could promote the electro-catalytic activity of MIEC cathodes as it would increase the ionic or protonic conductivity. However, a problem arising from use of LSCF is that it is chemically reactive with BCZY at temperatures higher than 1100 °C (17). Thus the two materials cannot be co-sintered or annealed at high temperatures.

2.3.2 K$_2$NiF$_4$ Structures

Oxides with the K$_2$NiF$_4$ structure are related to perovskites and of interest for SOFC cathodes because of their high diffusivity of the interstitial oxide ions (48). Ln$_2$NiO$_{4+\delta}$ (Ln = La, Pr, Nd) has attracted the most attention among cathode candidate materials from this family.

According to Yaremchenko et al., lanthanum nickel oxide has high oxygen mobility and low lattice expansion induced by variations in temperature and oxygen partial pressure (49). The activation energy of the diffusion in the *ab* plane is about 0.9 eV with a mechanism involving interstitial oxygen O_i^{2-} as the major diffusing species (50). La$_2$NiO$_{4+\delta}$ has high oxygen diffusion and surface exchange coefficient, $3.38*10^{-8}$ cm^2.s^{-1} and $1.75*10^{-7}$ cm.s^{-1} at 703 °C, respectively (51). The ionic conductivity is 0.02 S.cm^{-1} at 700°C (50), comparable with La$_x$Sr$_{1-x}$Co$_y$Fe$_{1-y}$O$_{3-\delta}$ (43) but the electronic conductivity is very low, 76 S.cm^{-1} at 800 °C (52). TEC of La$_2$NiO$_{4+\delta}$ compounds are in the range $11-13*10^{-6}$ K^{-1} (21).

As with perovskite oxides, researchers improved the properties of Ln$_2$NiO$_{4+\delta}$ through chemical substitution at both the La (A) and Ni (B) sites. Munnings et al. (53) found that La$_2$Ni$_{1-x}$Co$_x$O$_{4+\delta}$ had higher diffusion and surface exchange coefficients than the parent compound La$_2$NiO$_{4+\delta}$. The effects of strontium content on the electrical properties of La$_{2-x}$Sr$_x$NiO$_{4+\delta}$ have been reported and electrical conductivity increases with the value of x (54). Although preliminary results show that La$_2$NiO$_{4+\delta}$ and related compounds have most of

the desirable intrinsic properties needed for a good cathode, their performance to date in SOFCs falls below expectations.

2.3.3 Ordered Double Perovskites

In recent years, layered perovskites with the general formula $AA'B_2O_{5+\delta}$, where A = rare earth, A' = alkaline earth and B = Co, Mn, have been proposed for use as cathode materials for intermediate to low temperature SOFCs *(55-60)*.

Recent studies focused on two materials of this type, $GdBaCo_2O_{5+\delta}$ and $PrBaCo_2O_{5+\delta}$ because they have good oxygen transport properties, including high oxygen surface exchange coefficients and oxygen self-diffusion coefficient, together with high electronic conductivity.

Tarancon et al. studied the diffusion of oxygen and achieved high values of D_O, 10^{-9} $cm^2.s^{-1}$ at 700 °C for $GdBaCo_2O_{5+\delta}$ *(55)*. Kim et al. reported D_O in the order of 10^{-7} $cm^2.s^{-1}$ and k_O of 10^{-5} $cm.s^{-1}$ at 500 °C *(61)*.

Kim et al. *(62)* investigated $LnBaCo_2O_{5+\delta}$ (Ln = La, Nd, Sm, Gd and Y) and concluded that the oxygen content (the value of $5+\delta$), TEC, and catalytic activity each decrease with decreasing size of the Ln^{3+} ion from Ln = La to Ln = Y. Zhang et al. evaluated and ranked the performance of $LnBaCo_2O_{5+\delta}$ (Ln = La, Pr, Nd, Sm, Gd, and Y) *(56)*. The performance of different $LnBaCo_2O_{5+\delta}$ oxides was ranked as follows: $Pr^{3+} > Gd^{3+} > Nd^{3+} > Sm^{3+} > La^{3+} > Y^{3+}$.

As found for perovskite oxides, substitution is an effective strategy to modify the properties of double layered pervokites. Kim et al. studied the effect of strontium substitution in $GdBa_{1-x}Sr_xCo_2O_{5+\delta}$ *(59, 60)*. The results indicated

that strontium substitution improves the chemical stability with the electrolyte and the electrical conductivity.

2.3.4 Cathode Materials for Proton Conducting SOFCs

There are two research directions for cathode materials development for proton conducting SOFCS. The mainstream is to modify the cathode materials used in oxide ion conducting SOFCs. Very limited study was given to develop new materials, such as mixed protonic and electronic conductors.

LSCF was used in proton conducting SOFCs with a power density of 235 mW.cm^{-2} at 650 °C *(17)*. Yang et al. developed a composite cathode comprising mixed ionic and electronic conductor SSC and protonic conductor BCZY *(16)*. The effect of firing temperature was studied on the performance of single cell. A higher power density was obtained with SSC+BCZY cathode fired at 1000 °C compared to that fired at 900 and 1100 °C and the peak power density was 725 mW.cm^{-2} at 700 °C. A reaction between SSC and BCZY was identified. The potential application of $PrBaCo_2O_{5+\delta}$ double perovskite was investigated *(63)*. A peak power density of 520 mW.cm^{-2} at 700 °C and electrode polarization resistance of 0.06 $\Omega.cm^2$ were achieved for the single cell with the cathode fired at 950 °C.

Liu's group developed mixed protonic and electronic conductors: $BaCe_{0.5}Bi_{0.5}O_{3-\delta}$ *(64)* and $BaCe_{1-x}Fe_xO_{3-\delta}$ *(65)*. However, the study was limited to applying the cathode into a proton conducting SOFC, and evaluating the power density and resistance of the single cell. Researches, such as chemical

stability or chemical compatibility between the developed materials and electrolyte material, were not reported.

As these materials either have low power density or have issues such as, poor chemical compatibility, further researches on cathode development need be conducted.

Chapter 3 Experimental Approaches

3.1 Materials Preparation

3.1.1 Powders Preparation

Both the electrolyte BCZY and cathode materials LSCF and SCM were prepared using the citrate-nitrate combustion method.

The citrate-nitrate combustion process is a chemical solution method to prepare ceramic powders. It is effective to synthesize multi-component oxide materials (66). Typically, an aqueous solution of metal nitrates is mixed with a chelating agent citric acid and ammonium nitrate is added to the solution to facilitate the combustion process. The metal ions are uniformly distributed in the solution of chelate complexes formed from the polydentate ligand and the metal ions. The homogeneity of distribution within the resulting gel ensures that the subsequent combustion and high temperature calcination forms stoichiometric crystals as the final product.

The process is exemplified by the preparation of BCZY powders. The starting materials included $Ba(NO_3)_2$ (Alfa Aesar, 99+%), $Ce(NO_3)_3.6H_2O$ (Alfa Aesar, 99.5%), $Y(NO_3)_3.6H_2O$ (Alfa Aesar, 99.9%) and $ZrO(NO_3)_2.6.6H_2O$ (Aldrich, 99%) as metal precursors. The water content of zirconium (IV) oxynitrate hydrate was determined using thermogravimetric analysis. Stoichiometric amounts of metal nitrate were dissolved in de-ionized water. Citric acid (Alfa Aesar, 99.5+%) and NH_4NO_3 (Aldrich, 99.5+%) were

added as chelating agent and oxidant at a molar ratio of citric acid: total metal ions: NH_4NO_3 of 1.5: 1: 3. When a clear solution was obtained, ammonium hydroxide (Acros, 28-30% NH_3 in water) was added dropwise to adjust the pH to about 8. The final clear solution was heated on a hot plate to evaporate solvent until brown foam was formed and ignited. The as-combusted powder was then calcined between 1000 and 1500 °C for 10 h to get the desired phase. Figure 3.1 shows the synthesis process of BCZY in a flow chart. The prepared powders were characterized using X-ray diffraction.
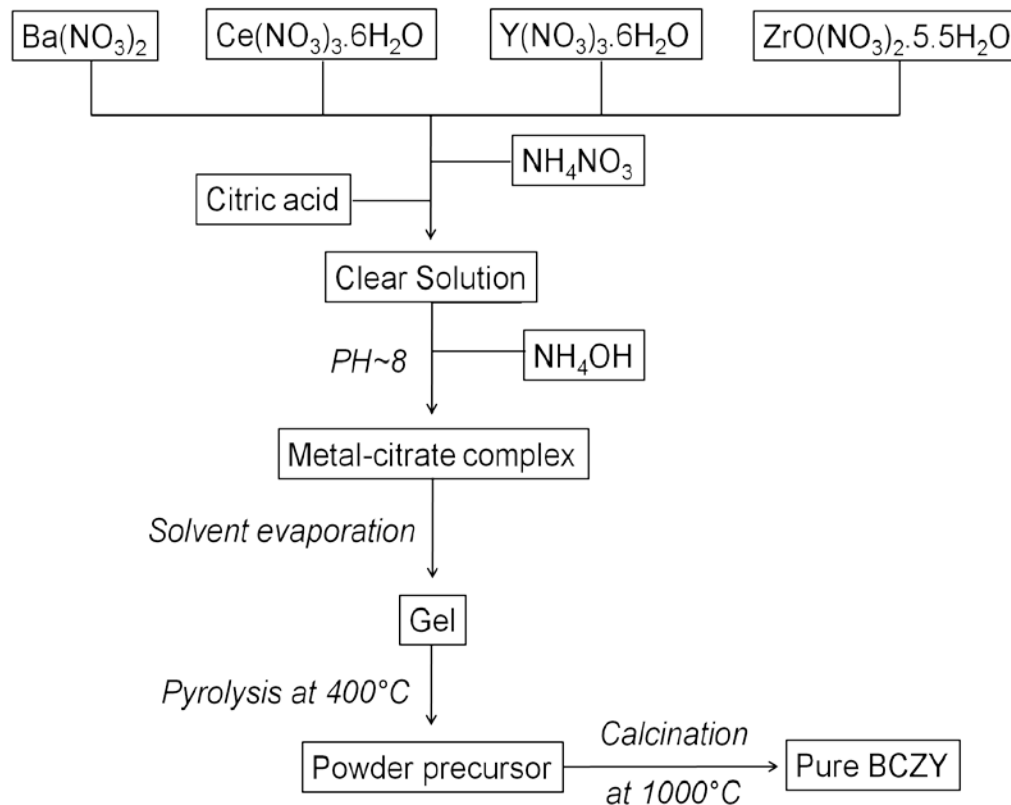
Figure 3.1. A flow chart illustrating the preparation procedure of the BCZY powders using the citrate-nitrate combustion method.

3.1.2 Densification of Electrolyte

As the electrolyte of proton conducting SOFCs, the electrolyte membrane should be dense enough to prevent fuel and oxidant gas crossover so that only protons are transported from anode to cathode through the electrolyte membrane. To get a dense electrolyte disk, the prepared BCZY powder was ground in isopropanol in a high energy ball milling machine (Fritsch Pulverisette 5) at 300 rpm for 1 h, blended with poly (vinyl alcohol) as binder

and pressed into a green disk with a 1.91cm die at a pressure of 5000 kg which was then sintered at 1500 °C for 10 h. Densification studies were performed by direct measurements of sample dimensions, the Archimedes method with water as medium, and scanning electronic microscopy after polishing the surfaces.

3.2 Fabrication of Anode Supported Thin Film Half Cells

The anode supported BCZY half cells were prepared by a suspension spin coating method. Powder consisting of green nickel oxide (Novamet), BCZY and graphite powder (Aldrich, <20 μm) as pore former with weight ratio 65:35:20 were thoroughly mixed in isopropanol in a high energy ball milling machine at 350 rpm for 1 h. The mixture was dried and pressed uniaxially into pellets with a 1.91cm die at a pressure of 2000 kg followed by firing at 1100 °C for 5 h to form porous substrates. BCZY electrolyte thin film was deposited on the substrates with a spin coating method. The flat substrates polished with sandpaper were fixed in a spin coating machine (Cookson electronics equipment specialty coating system). A thin layer of stable suspension was spin coated onto the substrate at a high spinning rate of 3600 rpm for 20 s and then dried, followed by evaporating and burning out part of the solvent with a heater. The thickness of the electrolyte could be controlled with the number of spin coating times. The suspension used for spin coating was a mixture of 20 wt% BCZY powders and 80 wt% organic vehicle obtained by putting the mixture in an ultrasonic machine for 30 min. The content of the organic vehicle is listed in

Table 3.1. The electrolyte coated anode substrates were then co-fired at 1400 °C

for 5 h to form a dense electrolyte thin film.

Table 3.1. Recipe of organic vehicle for spin coating

	Chemicals	Chemical Information	Content (wt %)
Binder	B76-PVB	Talas	5
Solvent	Isopropanol	Fisher, 99.9%	71
	α-Terpineol	Alfa Aesar, 96%	20
	Triethanolamine	Sigma-Aldrich, 99.9%	2
	Poly(ethylene glycol) 400	Aldrich	2

Half cells also were fabricated using co-pressing and co-firing method for
comparison, as this method is commonly used to prepare thin film proton
conducting SOFCs. A mixture of green nickel oxide, BCZY and graphite with
weight ratio 65:35:20 was co-pressed with BCZY powder. The bilayer was then
fired at 1400 °C for 5 h to densifiy the electrolyte.

3.3 Single Cell Fabrication and Assembly

Ag-perovskite cermet catalyst was prepared by mechanically mixing
commercial Ag powder (Alfa Aesar, spherical, -635 mesh, 99.9%) and a
prepared mixture of (LSCF+BCZY) (weight ratio 1:1) with a ball milling
machine. The slurry of the cathode material made with the prepared mixture

and commercially available vehicle ink (Fuel Cell Materials) was brush painted onto the BCZY surface of the anode supported bilayer pellet followed byfiring at 900 °C for 0.5 h. Ag paste was applied to cathode side and fired at 800 °C for 0.5 h to prepare the membrane electrode assembly (MEA).

The MEA was placed between two coaxial alumina tubes to form the anode and cathode compartments. Ceramic sealant (Ceramabond 503, Aremco) was applied on the outer tubes to seal the gas compartments (Figure 3.2). The internal diameter of the outer alumina tubes was 8 mm and the surface area of cathode was 0.32 cm^2. The cell then was heated in a Thermolyne F79300 tubular furnace to cure the sealant, and the temperature was adjusted to the selected operating temperature. For all single cell tests, 3 vol% H_2O/H_2 gas was fed into the anode chamber at a flow rate of 100 mL.min^{-1} as fuel, while air was supplied to the cathode chamber. Gold current collector wires (two probes) with spiral wound ends ran through the length of the inner tube.
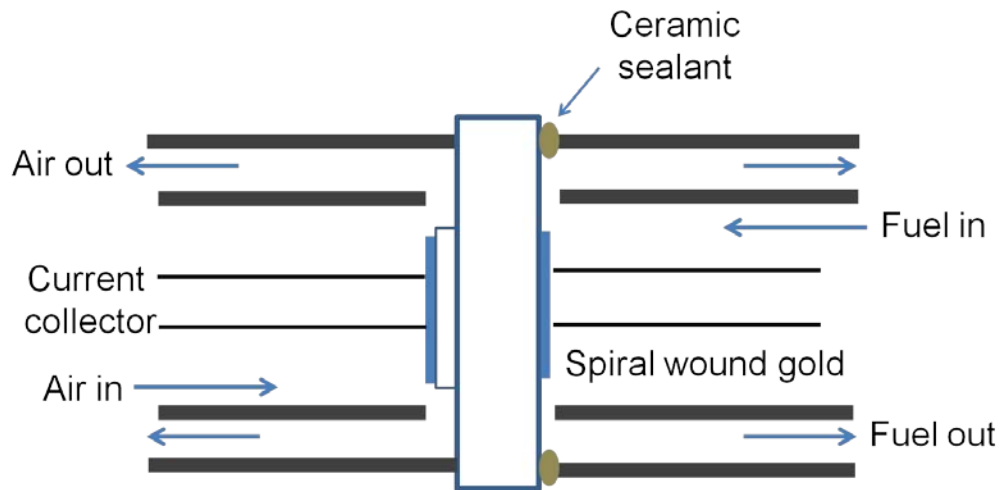
Figure 3.2. Schematic of fuel cell setup.

3.4 Characterization Methods

3.4.1 Powder X-Ray Diffraction (XRD)

XRD is an effective technique for identifying the phases in a sample. XRD data obtained in this study were collected at room temperature under ambient conditions with the Rigaku Ultima IV powder diffractometer using $CoK\alpha$ radiation (λ = 1.789Å). Measurements were conducted for all samples soon after synthesis to minimize any influence of water uptake. The scanning rate of the spectra was 2θ °.min^{-1}. The commercially available software Jade was used to identify phases in the sample.

3.4.2 Thermal Analysis

Thermogravimetric analysis (TGA) was performed using a TA Instruments SDT Q600 to evaluate the chemical stability of the prepared electrolyte BCZY in CO_2-containing atmosphere. Precisely measured powder samples of about 20 mg were placed in an alumina cup (90 μL) in CO_2/He flow (CO_2 = 2 mL.min^{-1}; He = 100 mL.min^{-1}). The sample was heated at a rate of 10 °C.min^{-1} from room temperature to 1200 °C.

3.4.3 Scanning Electronic Microscope (SEM)

Microstructure and morphology of particles and sintered products were determined with a Zeiss SEM. The cross section was obtained by fracturing the sample. A conducting carbon tape was used to ensure the electron conductivity.

A thin layer of gold was sputtered onto the samples because the perovskite ceramics were non-conductive at room temperature.

3.5 Conductivity Testing for Electrolyte

The dense electrolyte membrane obtained by sintering the green pellet at 1500 °C for 10 h was polished to a thickness of 1.2 mm using sandpapers of grade 400 and 600. Gold paste with area of 0.97 cm^{-2} was applied onto both sides of the membrane as current collector, and then heat treated at 900 °C for 30 min to burn out organic binders and form the MEA for conductivity measurements. The MEA with a two-electrode cell configuration under symmetrical cell conditions was assembled in a quartz tube with gold wire and mesh as current collector.

Conductivity testing was performed using an impedance system that consisted of a Solartron 1255 HF frequency response analyzer and a Solartron 1287 electrochemical interface. Conductivity measurements were performed from 500 to 750 °C at 50 °C intervals with a 10 mV applied voltage. Electrochemical impedance spectra (EIS) were collected in 10% H_2/He humidified atmosphere (3 vol% H_2O) by bubbling the gas through water at room temperature and analyzed with the Zview modelling software (Scribner Associates, Inc.).

3.6 Electrochemical Measurements for Single Cells

Electrode performance was investigated for the single cell configuration with an electrochemical workstation based on a Solartron 1287 potentiostat and a Solartron 1255 frequency response analyzer. The tests were conducted using a four electrode set-up from 550 to 700 °C at 50 °C intervals. Air and humidified H_2 were fed to cathode and anode at atmospheric pressure with flow rate of 100 mL/min. Potentiodynamic mode was used when performing current-potential measurements. Potentiostatic mode was used to monitor the current stability at the set potential of 0.75 V. Impedance measurements were conducted under open circuit voltage (OCV) conditions. The frequency was varied from 0.01 Hz to 1 MHz with signal amplitude of 10 mV.

Chapter 4   Results and Discussion

To optimize performance of proton conducting SOFCs requires an extensive knowledge of the behaviour of the electrolyte, preparation of thin film single cells and development of cathode materials. To this end, the conductivity and chemical stability of electrolyte BCZY now have been evaluated. Thin film electrolyte was prepared and characterized. The performances of two cathode materials were determined in anode supported thin film button cells.

4.1. Electrolyte Preparation and Characterization

4.1.1 Introduction

Since Takahashi and Iwahara determined the proton conductive properties of some perovskite oxides in 1980 *(67)*, proton conducting materials and their properties have been investigated extensively *(12, 68-73)*. Among the proton conductors studied so far, $BaCeO_3$-based perovskite oxides exhibit the best conductivity under a humidified hydrogen-containing atmosphere in the temperature range 500-750 °C. Among them, Y-doped $BaCeO_3$ (BCY) ceramics have the conductivity of about $4*10^{-2}$ S.cm^{-1} at 700 °C when it is doped with 20% Y ($BaCe_{0.8}Y_{0.2}O_{3-\delta}$) *(71)*. The partial substitution of tetravalent Ce with trivalent cations of Y introduces oxide ion vacancies to the perovskite structure, as described in Kroger-Vink notation by *(74)*:

$$2Ce_{Ce}^{X} + Y_2O_3 + O_O^{X} \rightarrow 2Y_{Ce}' + V_O^{\cdot\cdot} + 2CeO_2 \qquad (4\text{-}1)$$
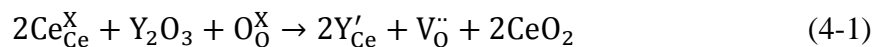
Oxygen vacancies which are the main defects in the structure, will be incorporated by transfer of protons from water according to the reaction *(11)*:

$$H_2O + V_O^{\cdot\cdot} + O_O^X \rightarrow 2OH_O^{\cdot} \qquad (4\text{-}2)$$

The protons migrate as lone protons between stationary oxide ions in oxides in the Grotthuss mechanism shown in Figure 4.1 *(75)*. Proton migrations in perovskites have activation energies ranging from 0.39 eV to 0.74 eV with the value of about 0.5 eV for Y doped BaCeO₃ oxides *(76)*.
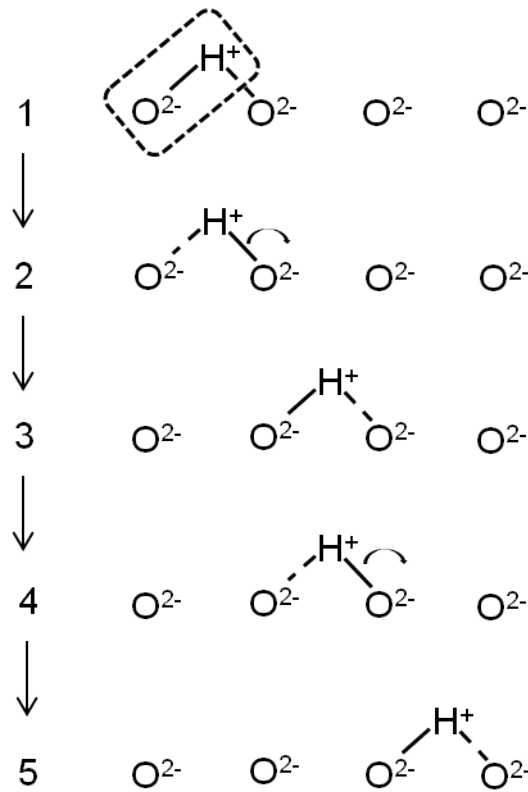
Figure 4.1. Illustration of proton migration in perovskite type oxides *(75)*.

While the high conductivity of $BaCeO_3$-based perovskite is good, the stability of these oxides is of great issue. The chemical stability of $BaCeO_3$-based perovskite in CO_2 and H_2O-containing atmospheres, which is a prerequisite for their application as an electrolyte, is very low *(77)*. Recent studies show that partial substitution of Ce by Zr greatly improves the stability of BCY in CO_2 atmospheres *(12, 78)*. In this project, BCZY was employed as the electrolyte as it exhibits both high proton conductivity and good chemical stability against H_2O and CO_2 *(12)*.

4.1.2 Characterization of BCZY Electrolyte

The metal ions required to form BCZY were well distributed in the preparation solution, and were chelated as citrates. Ammonium nitrate was added to the solution to promote ignition and oxidation. When the mixture was dried and ignited in air, fine powders were obtained from which final pure phase oxide was obtained after high temperature calcination in air. Figure 4.2 illustrates the whole combustion processes.
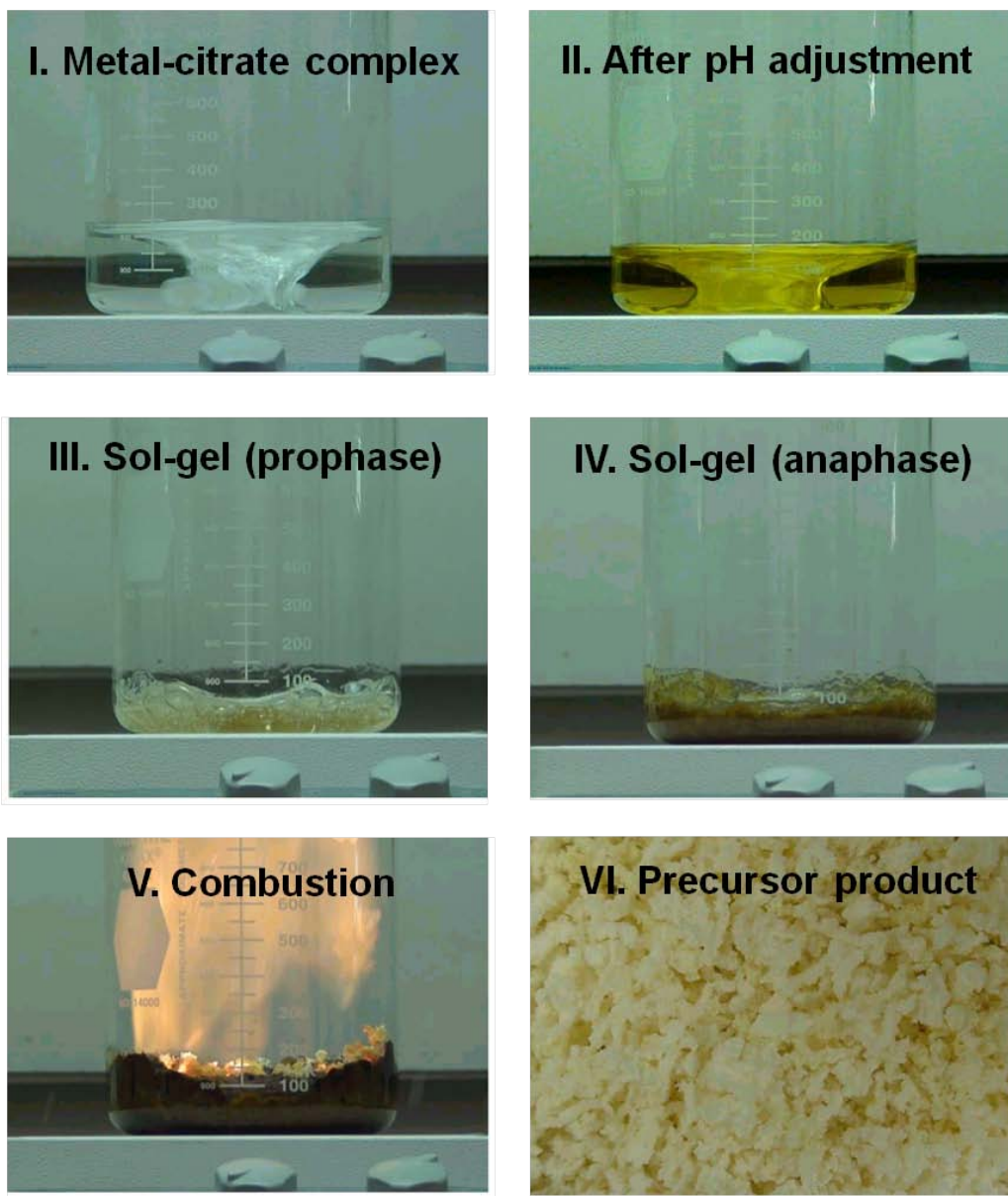
Figure 4.2. The citrate-nitrate combustion process.

The room temperature XRD pattern of the prepared powders (Figure 4.3) showed that a single phase composite oxide BCZY was obtained at 1000 °C. XRD patterns of the oxides calcined at higher temperatures showed that the perovskite structure was stable in air at temperatures up to 1500°C.
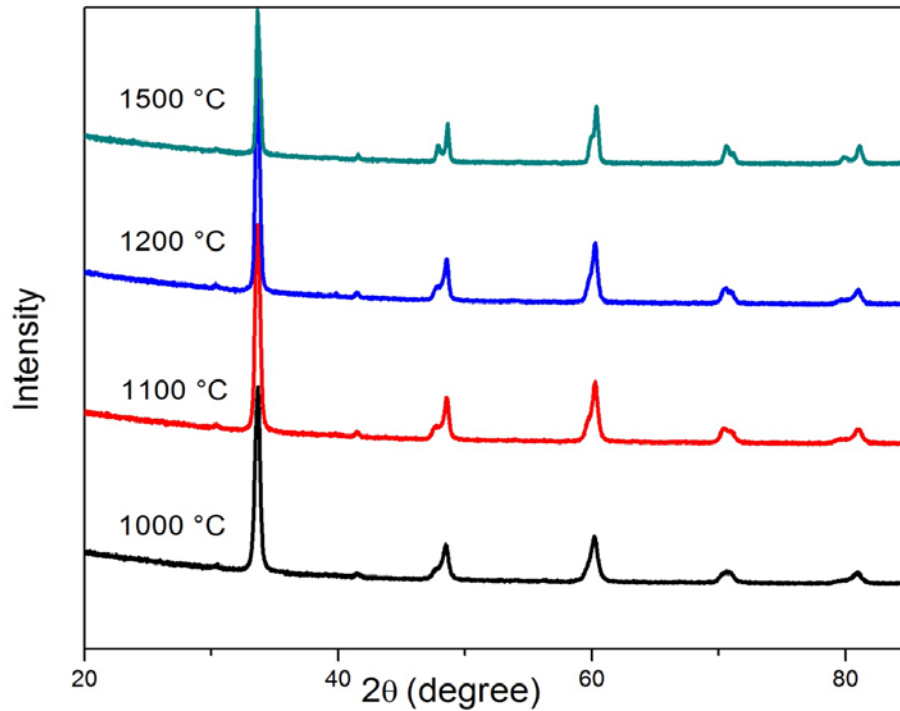
Figure 4.3. XRD patterns of BCZY powders prepared using the citrate-nitrate combustion method calcined at different temperatures in air.

To determine the particle size and morphology of the prepared electrolyte BCZY powders, the powders calcined at 1000 °C were dispersed in ethanol and examined using SEM. The micrograph in Figure 4.4 shows that the particles were uniformly distributed of sub-micron sizes. It indicated that the mixing of the metal cations in a solution and the large amount of gas evolved during the combustion process facilitated formation of the fine, highly dispersed sub-micron powders.
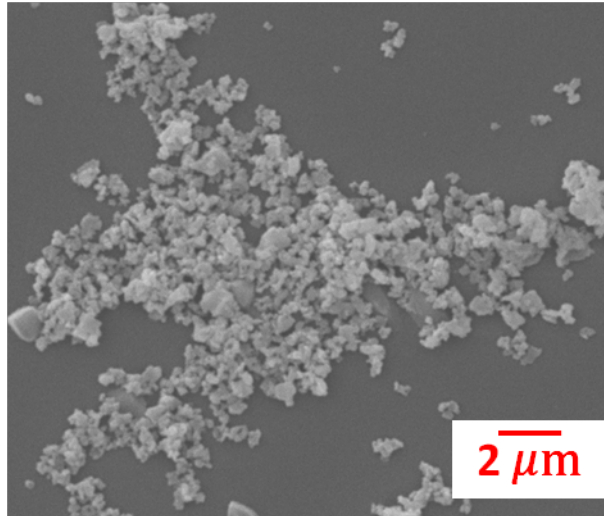
Figure 4.4. SEM image of BCZY powders obtained using the citrate-nitrate combustion method and calcined at 1000 °C.

While BCY demonstrates the highest conductivity among oxide proton conductors, it is unstable in CO_2-containing atmospheres at elevated temperatures (77). It reacts readily with CO_2 to form CeO_2 and $BaCO_3$, which hinders its practical application as an electrolyte in proton conducting SOFCs. It has been proven that the addition of Zr to $BaCeO_3$-based perovskite oxide improves its chemical stability against reaction with CO_2 (12). Figure 4.5 compares the TGA curves of $BaCe_{0.85}Y_{0.15}O_{3-\delta}$ and BCZY determined in CO_2-containing atmosphere. When the temperature was above 500 °C, there was a large weight uptake to a maximum of 13% for $BaCe_{0.85}Y_{0.15}O_{3-\delta}$ due to formation of $BaCO_3$. In contrast, no significant weight uptake took place for BCZY when heated in a CO_2-containing atmosphere, which confirms that Zr doping improves the chemical stability of $BaCeO_3$ at high temperatures.
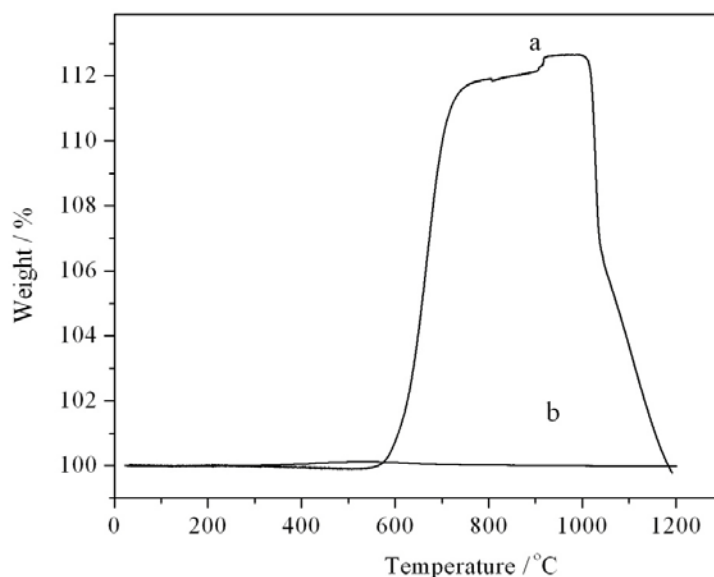
Figure 4.5. TGA curves of (a) $BaCe_{0.85}Y_{0.15}O_{3-\delta}$, and (b) BCZY in CO_2-containing atmosphere.

Though the chemical stability in a CO_2-containing atmosphere improves with the addition of Zr, the sinterability of the doped oxides decreases. Basically, a high temperature and long sintering time are required to get a dense disk for this class of materials. The conditions of 1500 °C and 10 h were chosen for the first sinterability studies. The density determined using Archimedes method was 5.91 $g.cm^{-3}$. The theoretical densities of $BaCe_{0.6}Zr_{0.3}Y_{0.1}O_{3-\delta}$ and $BaCe_{0.9}Y_{0.1}O_{3-\delta}$ are 6.23 and 6.12 $g.cm^{-3}$ *(79)*. Therefore, it is reasonable to assume that the theoretical density of BCZY is about 6.2 $g.cm^{-3}$, from which the relative density of the prepared electrolyte disk was calculated to be 95%, sufficiently dense for a disk to serve as the electrolyte of SOFCs. Figure 4.6 shows the surface and cross-sectional morphologies of the BCZY pellet after

sintering at 1500 °C. The electrolyte was well densfied and there were only very few small closed pores.
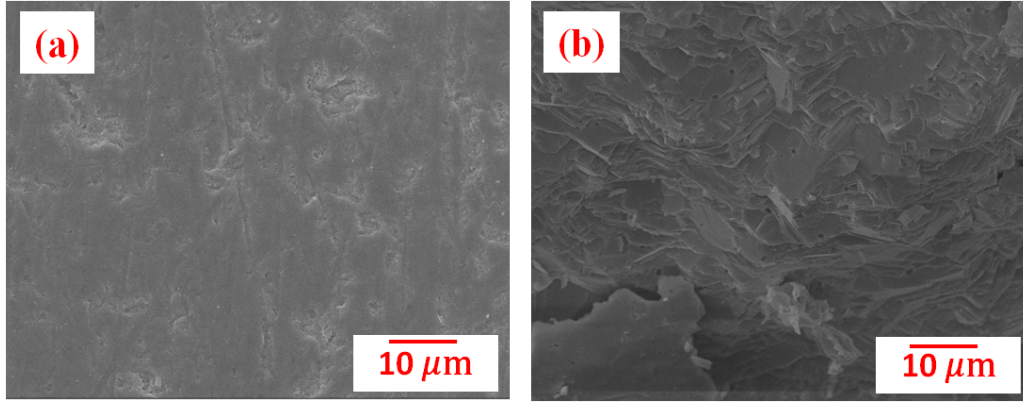
Figure 4.6. Morphology of the dense BCZY disk sintered at 1500 °C for 10 h (a) surface morphology, (b) cross-sectional morphology.

4.1.3 Conductivity Testing for Electrolyte

The total conductivity of BCZY was calculated by converting the resistance to the conductivity (σ), based on sample geometry *(3)*:

$$\sigma = \frac{l}{RA} \tag{4-3}$$

where l is the sample thickness, A is the sample area, and R is the ohmic resistance of the sample determined as the high frequency intersect with the real axis of the electrochemical impedance spectra on a Nyquist plot. An Arrhenius plot of the conductivity was obtained from the following Equation *(3)*:

$$\sigma = \frac{\sigma_0}{T} \cdot e^{-E_a/kT} \tag{4-4}$$

where σ_0 is the pre-exponential factor, T is the absolute temperature, k is the Boltzman constant and E_a is the activation energy for proton conduction.

Due to the high oxygen vacancy concentration, which incorporates protons upon exposure to humidity, BCZY membranes provided good conductivity: 11, 20 and 33 mS.cm^{-1} at 550, 650 and 750 °C, respectively, which are slightly higher than the reported values *(12)*. Figure 4.7 is the Arrhenius plot of the oxide BCZY in the temperature range 500-750 °C in a flowing humidified 10% H$_2$/He atmosphere in which the process of water vapour adsorption is expected to happen and thereby enable reaction with oxide ion vacancies and lattice oxygen to produce hydroxide species (Equation 4-2). The activation energy for proton hopping in the perovskite BCZY was 0.43 eV, determined from the Arrhenius plot, which is lower than the value Lin et al. obtained *(63)*.
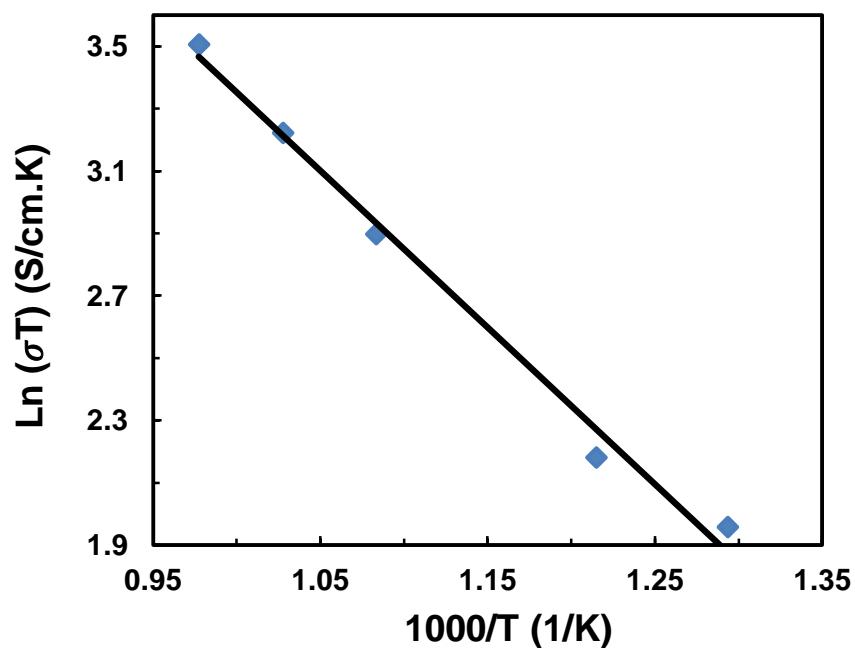
Figure 4.7. Arrhenius plot of conductivity of BCZY in humidified 10% H_2/He atmosphere.

4.1.4 Summary of BCZY Preparation and Characterization

Pure phase doped barium cerate BCZY powders for a proton conducting electrolyte were synthesized using the citrate-nitrate combustion method at 1000 °C. The prepared electrolyte has a good combination of chemical stability against reaction with CO_2, sinterability and conductivity. Pellets with densities about 95% of the theoretical value were obtained by sintering the prepared sub-micron powders at 1500 °C for 10 h. Excellent conductivities of the BCZY membranes were obtained in humidified 10% H_2/He: 11, 20 and 33 mS.cm^{-1} at 550, 650 and 750 °C, respectively.

4.2 Thin Film Half Cells Characterization

One key factor that affects the performance of the fuel cell is the ohmic loss due to the charge transport, mainly ion transport through the electrolyte. Ohmic loss can be minimized by employing high-conductivity materials and making electrolytes as thin as possible as the resistance scales with thickness of the electrolyte. Normalizing the conductivity, area-specific resistance (ASR) is expressed by the following relationship *(3)*:

$$ASR = \frac{l}{\sigma} \tag{4-5}$$

where l is the thickness of the electrolyte and σ is the conductivity of the material. Therefore, the shortest path possible for ions between the anode and the cathode is desired which means the electrolyte of the fuel cell should be as thin as possible, without jeopardizing physical integrity. Although the performance of the fuel cell improves with reducing the thickness of electrolyte, thin film fuel cells bring up new problems. The thickness of the electrolyte is limited with practical issues including mechanical integrity, non-uniformities in composition and thickness, and gas crossover.

Ni-perovskite cermet is by far the most active anode for current SOFCs using H_2 as fuel. Ni-YSZ is the most commonly used anode material for oxide ion conducting SOFCs as it meets the requirements of anode materials. Metallic Ni is an excellent catalyst for the oxidation of hydrogen and provides electronic conductivity for the anode, while the addition of YSZ increases the oxide ionic conductivity, which in turn enlarges the extent of the triple phase boundary *(80-*

82). Many studies related to development of proton conducting SOFCs describe cathodes based on the Ni-BCZY cermet anode *(16, 22, 63)*.

In this project, Ni-BCZY was used as the anode catalyst, and a thin film electrolyte as shown in Figure 4.8 was prepared with a novel spin coating method from which a uniform and easily controllable thin layer of the electrolyte was obtained.
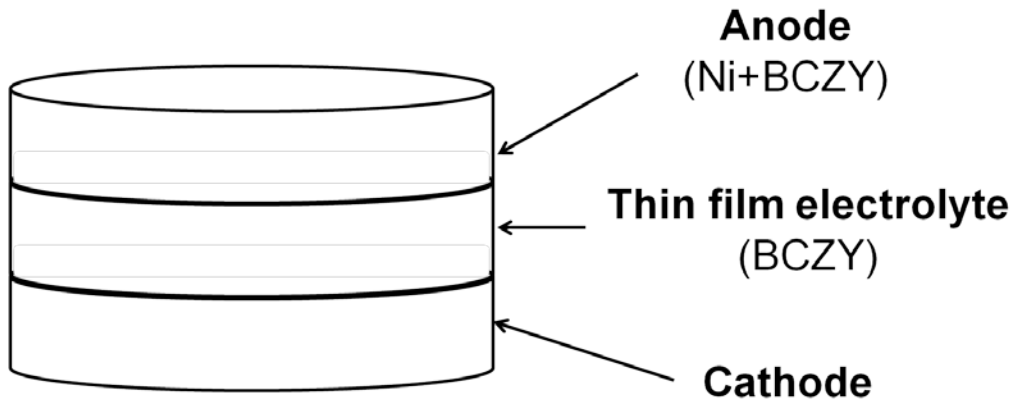
Figure 4.8. Illustration of thin film SOFC design (not proportional).

The approach used here to develop the thin film was to use a NiO+BCZY disk as the anode and deposition substrate for the fuel cell. The electrolyte layer was deposited on the substrate using spin coating technique to form a dense layer after sintering at high temperature.

Figure 4.9 compares pictures of the sintered bilayer half cells prepared by spin coating (right picture) and the co-pressing and co-sintering method (left picture). Both the top view in Figure 4.9 (a) and side view in Figure 4.9 (b)

show that the half cell prepared using the co-pressing and co-sintering method was bent toward the anode side due to the shrinkage difference between anode substrate and electrolyte BCZY after sintering at high temperature. This shrinkage difference not only came from the intrinsic difference between thermal expansion coefficients of the anode mixture of nickel oxide and BCZY and the electrolyte BCZY but also from the effects of burning out graphite that was admixed into the anode mixture as a pore former. Although it is possible to test a distorted cell in lab scale experiments, it is impractical to use them in an application. The other problem with a co-pressing and co-firing method is that it is difficult to get a uniform layer of electrolyte. On the other hand, the bilayer half cell prepared by spin coating was flat, as the shape or the bending properties of the half cell could be controlled by adjusting the prefiring temperature of the substrate, the co-firing temperature or the slurry recipe. In this project, the prefiring temperature was chosen as the variable with the final sintering temperature fixed at 1400°C and the slurry as mentioned before.
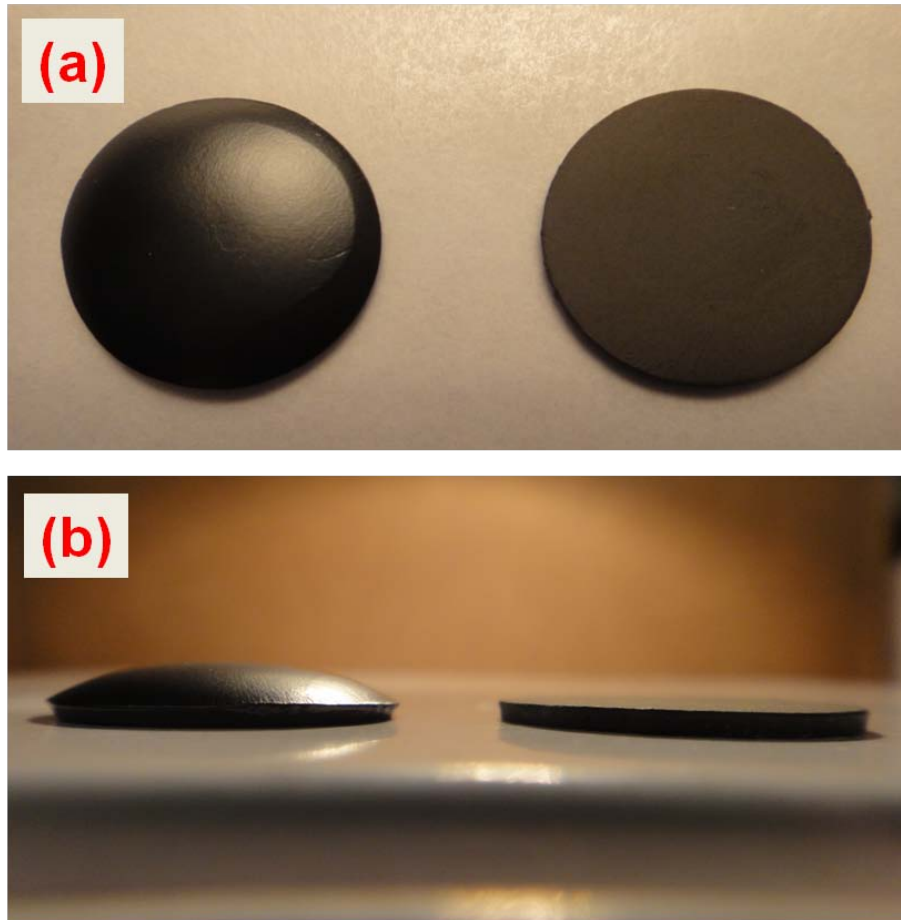
Figure 4.9. Comparison of half cells after sintering at 1400 °C (a) top view, (b) side view. Left: co-pressing and co-firing method; right: spin coating method.

Figure 4.10 lists the three half cell configuration effects that may happen after high temperature sintering. Only when the anode substrate and electrolyte shrinkages are the same is the cell flat, as shown in Figure 4.10 (b). If the electrolyte has higher shrinkage than the anode substrate, the cell tends to bend towards the electrolyte side as shown in Figure 4.10 (a). In this case, the pre-firing temperature of the anode substrate can be decreased to synchronize the shrinkage and so obtain a flat cell, as shown in Fig 4.10 (b). The case

illustrated in Figure 4.10 (c) happens when the anode substrate shrinks more than the electrolyte. The pre-firing temperature of the anode substrate should be increased to decrease its shrinkage so a flat half cell can be obtained. After several trial and error experiments, 1100 °C was identified as the prefiring temperature to obtain flat button cells after spin coating with the suspension mentioned previously in the table, then heating.
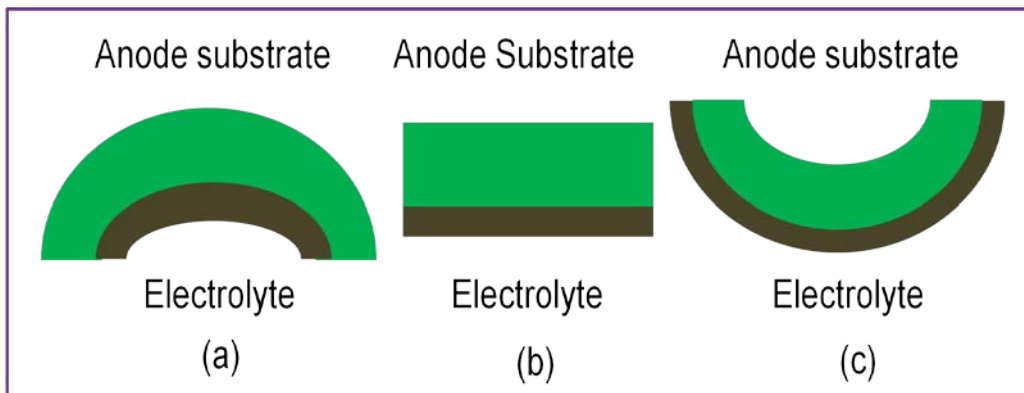
Figure 4.10. The three half cell configurations after sintering: (a) bending toward electrolyte; (b) no bending; (c) bending toward anode substrate.

Figure 4.11 shows a typical SEM image of the anode supported fuel cell fabricated by the spin coating method with six coatings after sintering at 1400 °C before testing. Few pores were detected within the NiO anode substrate before testing. However, during running of the cell, nickel oxide was reduced to nickel and produced pores available for gas diffusion. The cross-sectional SEM images indicated that the BCZY electrolyte film did not have any noticeable connected pores, even though inner isolated pores were visible.

The thickness of the electrolyte film was about 40 μm after six spin coatings. The SEM images shown in Figure 4.11 also revealed that the electrolyte film was well adhered to the anode substrate, without any cracking or delamination before fuel cell testing. OCV of single cells and stability of data during fuel cell testing also proved that the electrolyte was dense enough to prevent gas crossover. Based on these results, electrolytes with six coated layers were employed for the following experiments.
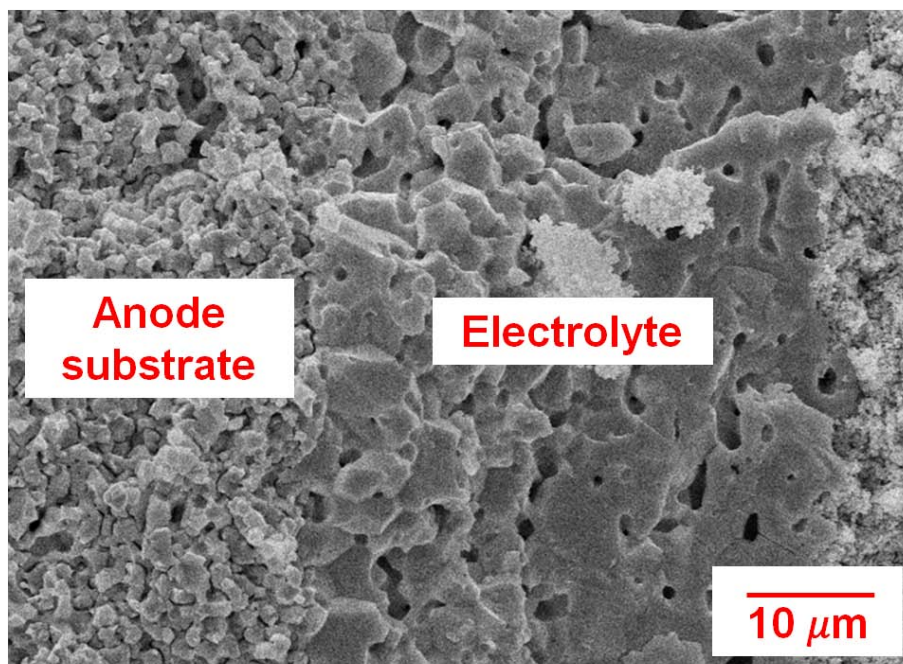
Figure 4.11. Cross-sectional SEM image of the anode supported half cell prepared using spin coating method after firing at 1400 °C with six layers of suspension applied on the substrate.

To sum up, the spin coating method efficiently produced flat button fuel cells with a thin, dense layer of electrolyte, and the thickness of the electrolyte layer was proportional to the number of coatings. A dense electrolyte layer was obtained, with few noticeable connected inner pores and no contiguous channels, by sintering the half cells at 1400 °C. Flat button cells were obtained by prefiring the anode substrate at 1100 °C. The thickness of the electrolyte was 40 μm with six spin coating. Thus six times of spin coating was chosen to be used for the electrolytes, as the layer so produced was very thin, so as to minimize resistance, but sufficiently dense to prevent gas permeation.

4.3 Ag-(LSCF+BCZY) as Cathode Catalyst

4.3.1 Introduction

One critical means to improve commercialization of SOFC technology is to lower the operating temperature *(6)*. Although proton conducting SOFCs can operate at lower temperature when compared to oxide ion conducting SOFCs due to higher conductivity of protonic electrolytes than well-known oxide ionic conductors, such as doped ceria *(12, 83)*, the performances to date of proton conducting SOFCs still are lower than those of optimized oxide ion conducting SOFCs. These phenomena may be ascribed to an increase of electrode polarization and electrolyte resistance at reduced operating temperature *(16)*. The electrolyte (ionic) resistance can be reduced dramatically by using a thin film electrolyte on an anode support structure *(84)*. However, the performance is still limited, mainly as a consequence of cathode polarization. Thus, development of improved cathodes is of great importance for low-to-intermediate temperature SOFCs.

To work well as a cathode catalyst for protonic SOFCs, it should have the following characteristics:

- High electronic, protonic and oxide ionic conductivity.
- High electro-catalytic activity for reduction of oxygen.
- Chemically stable in oxidizing humid atmospheres and at high temperatures.

- Chemically and thermally compatible with other components of the fuel cell.

However, it is almost impossible for one material to satisfy all these requirements as the cathode material. Researchers have been devoting their energy to improving cathode performance based on cathode materials commonly used in oxide ion conducting SOFCs. Protonic conductivity is introduced by adding proton conducting materials, often the same materials used as an electrolyte, to the cathode oxide *(17, 63, 85)*. Noble metals such as Ag, Pt and Pd are used in admixtures with the oxide cathodes to improve the cathode performance. The introduction of precious metals into oxide cathodes may increase the electronic conductivity and the electro-catalytic activity for the oxygen reduction reaction due to the high electronic conductivity of precious metals and the synergetic effect of precious metals and oxide electrodes *(86-89)*.

LSCF perovskite oxide is a promising cathode material for SOFCs operated at intermediate temperature *(90)*. The performance of Ni-YSZ|$Ce_{0.9}Gd_{0.1}O_{1.95}$|LSCF cell was investigated in the temperature range 550-650 °C *(86)*. Peak power densities of 140 mW.cm^{-2} and 80 mW.cm^{-2} were observed at 650 °C and 600 °C, respectively. The addition of Pd to the LSCF cathode was found to decrease the overall cell resistance by 15% at 650 °C and 40% at 550 °C *(86)*. However, the fast deterioration of cell performance with addition of Pd *(87)* and the price of the Pd led to the research into alternative noble metals. Ag is the least expensive among the noble metal family, and has

good catalytic activity and high electrical conductivity which make it an excellent candidate for use in SOFC cathodes. Performance of Ag-$La_{0.6}Sr_{0.4}Co_{0.8}Fe_{0.2}O_3$-$Ce_{0.8}Gd_{0.2}O_{1.9}$ cathode on a $Ce_{0.8}Sm_{0.2}O_{1.9}$ electrolyte was studied using the AC impedance method at steady state with various DC bias currents *(88)*. The addition of Ag into the LSCF-GDC composite electrode improved the catalytic activity for oxygen reduction. Ag impregnated cathodes have greatly improved the performance of micro-tubular SOFCs at intermediate temperature. The peak power density for the Ni-$(ZrO_2)_{0.89}(Sc_2O_3)_{0.1}(CeO_2)_{0.01}(ScSZ)|ScSZ|GDC|LSCF$ single tubular cell without Ag loading at 550 °C was 110 mW.cm^{-2} and significantly increased to 490 mW.cm^{-2} with Ag impregnation *(89)*.

Herein, I evaluated the electrochemical performance of Ag-modified LSCF+BCZY as the cathode catalyst in a proton conducting SOFC. BCZY was chosen as the electrolyte as it is more stable than BCY against adverse reactions with CO_2 and H_2O-containing atmospheres.

4.3.2 Cathode Material Characterization

As shown in Figure 4.12, a single perovskite phase structure of LSCF powder was obtained using the citrate-nitrate combustion method at 700 °C, 750 °C, and 800 °C for 2 h. No peaks attributed to impurities were detected using XRD.
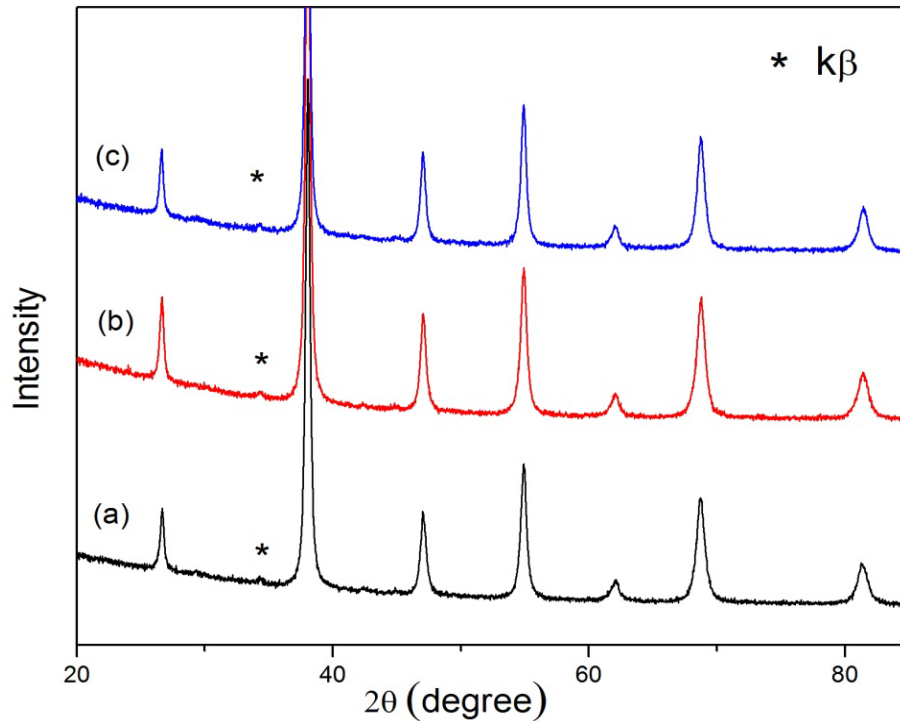
Figure 4.12. XRD pattern of LSCF powder calcined for 2 h at (a) 700 °C, (b) 750 °C, and (c) 800 °C.

To determine the compatibility between LSCF and electrolyte BCZY, mixed powders of LSCF and BCZY with weight ratio of 50:50 was fired at 1000 °C and 1100 °C for 10 h. There was no significant amount of reaction between BCZY and LSCF at 1000 °C. As shown in Figure 4.13, the XRD patterns of the mixture after the calcination at 1000 °C can be indexed well based on a physical mixture of LSCF and BCZY. However, when the temperature was increased to 1100 °C, a small peak of unidentified phase was detected in the XRD pattern. Thus, the firing temperature of cathode should not go higher than 1100 °C to avoid any reaction between the cathode and electrolyte layers.
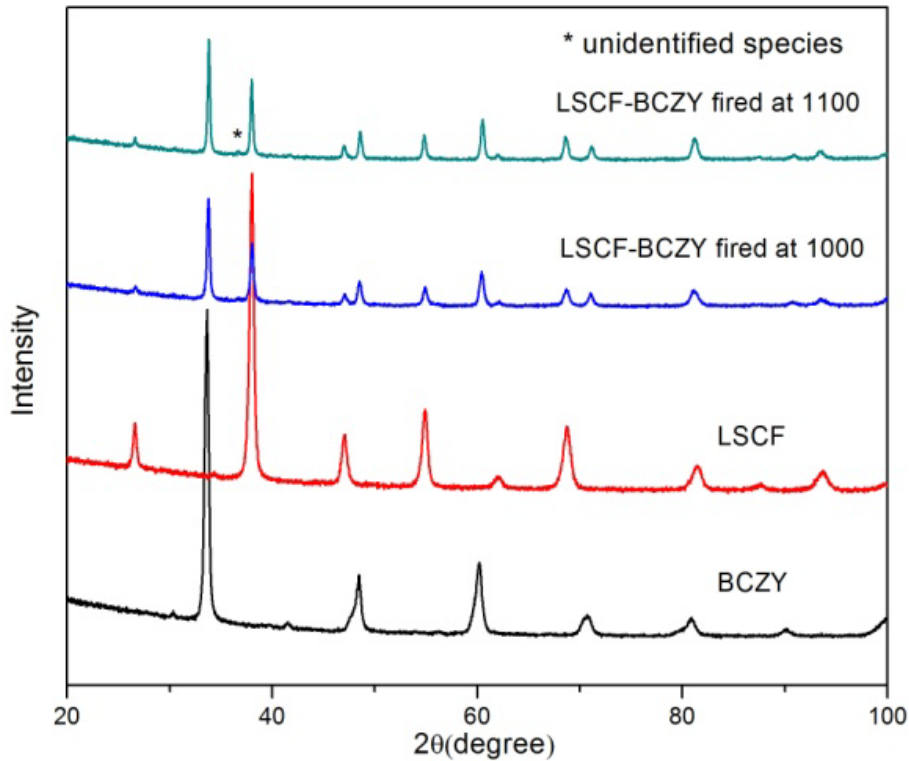
Figure 4.13. XRD patterns of BCZY, LSCF and mixed powder of LSCF and BCZY at a weight ratio of 50:50 after calcination at 1000 and 1100 °C.

In a proton conducting SOFC water is produced at the cathode side when protons which are produced at the anode side and transported through the electrolyte react with oxygen species at the cathode side. Therefore, it is necessary that the cathode material be stable under a humid atmosphere. Figure 4.14 shows the XRD patterns of the as prepared LSCF and LSCF exposed to 15 vol% H2O/air at 700 °C for 20 h. No new phases were detected in the XRD patterns, which showed that LSCF was stable against reaction in a humid atmosphere.
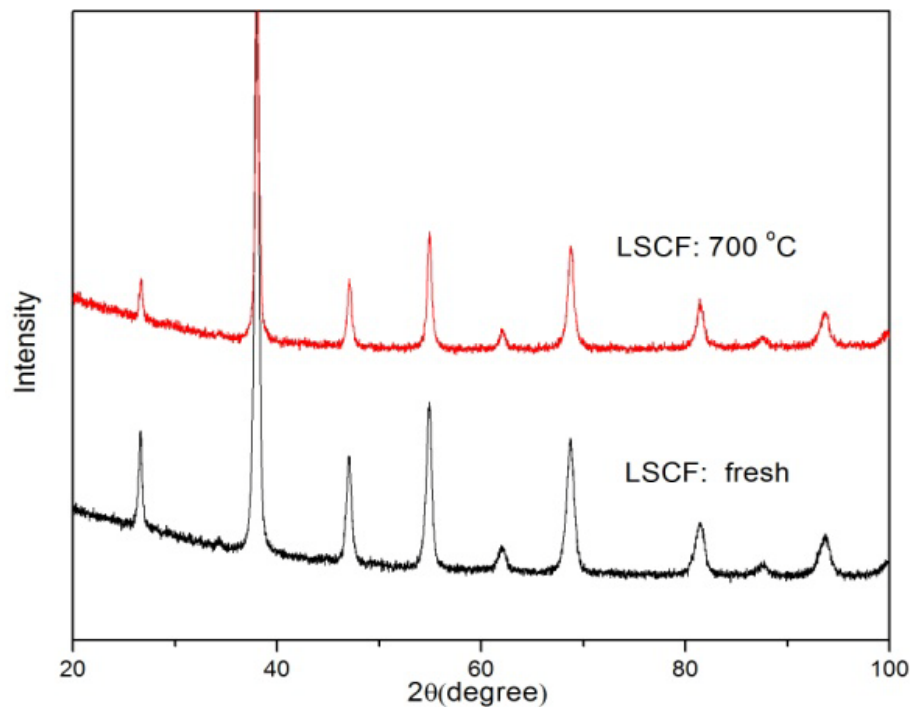
Figure 4.14. XRD patterns of LSCF before and after exposed to 15 vol% H$_2$O/air at 700 °C for 20 h.

4.3.3 Fabrication of the Anode Supported Single Cells

To prepare the Ag-modified LSCF cathode, Ag powder, LSCF and BCZY were mechanically mixed to obtain the cathode powder. The cathode slurry obtain by mixing the powder and commercial vehicle ink with a pestle was brush painted onto the BCZY electrolyte surface and then fired at 900 °C for 0.5 h to ensure the electrode layer adhered to the electrolyte surface. The firing temperature was limited by the melting temperature of Ag (961 °C) to prevent agglomeration of the Ag species which can block the transport path for gaseous oxygen. Thus the temperature was lower than commonly used firing

temperatures of electrodes, typically between 1000 and 1200 °C. While a low temperature may result in poor attachment between cathode and electrolyte, a low temperature also may alleviate complications arising from chemical incompatibility between the electrode and the electrolyte layers.

Shown in Figure 4.15 are the cross-sectional SEM images of the cathode with different Ag contents fired at 900 °C after single cell tests. The cathode layer was well attached to the electrolyte layer, which was not found for the case without Ag addition at such a low temperature. The low melting point of Ag facilitated the firing properties of the cathode, and the ceramic impeded grain growth of Ag to some extent. The cathode grains were very fine due to the low melting temperature, and the cathode was porous. Fabrication of the cathode mechanically mixing materials has its own drawbacks. It is difficult to get fine Ag grains and uniformly distributed Ag, LSCF and BCZY within the cathode. The issue can be solved using an impregnation method *(91)* by impregnating LSCF and Ag into the BCZY porous structure. Low firing temperature of impregnated LSCF and Ag can result in a good cathode structure.
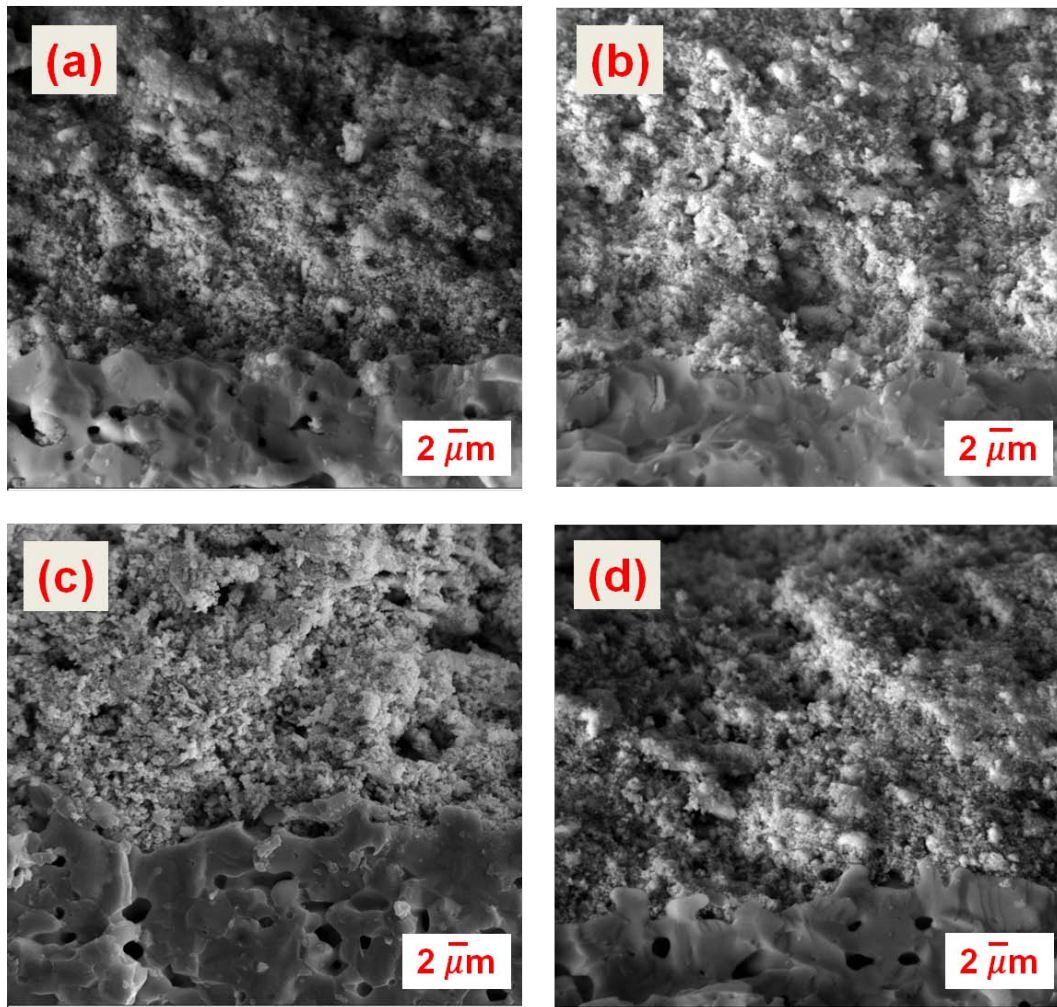
Figure 4.15. Cross-sectional SEM morphologies of Ag-(LSCF+BCZY) cathode (a) 10 wt% Ag; (b) 20 wt% Ag; (c) 40 wt% Ag; and (d) 50 wt% Ag.

4.3.4 Electrochemical Performance of Single Cells

The oxygen reduction reaction on cathodes of oxide ion conducting SOFCs has been extensively studied. It is well known that MIECs can extend the electrochemically active sites to the cathode surface beyond TPB. When

using a MIEC on a protonic SOFC, the reaction sites are limited to TPB where oxygen species, electrons from cathode, and protons from electrolyte meet. In order to extend the reaction sites, a potential cathode must have protonic, oxide ionic and electronic conductivity. A cathode material conducting protons, oxide ions and electrons can extend reduction reaction sites from the electrolyte/cathode interface to the entire cathode surface. Unfortunately, a single phase protonic, oxide ionic and electronic conductor has not been developed. The idea of a composite cathode with a MIEC and a protonic conductor may tailor the properties of a potential cathode for protonic SOFCs. The performance of a composite cathode may be further improved with the addition of Ag which is a good electronic conductor.

In order to evaluate the performance of the composite cathode, thin film button cells with the configuration of NiO+BCZY|BCZY|composite cathode were tested under single cell conditions. The dense electrolyte on a porous anode substrate was an important factor for cell performance. In this study, an anode Ni+BCZY supported BCZY thin film layer was successfully prepared using the spin coating technique.

Figure 4.16 compares the peak power densities of single cells with different Ag contents. The performance improved with an increase of Ag content in the cathode at a low amount up to 10 wt% Ag, which is ascribed to the decrease of ohmic resistance. However, with further increase of Ag content the performance deteriorated. This trend becomes prominent at elevated temperatures. This may be due to that too much Ag in the cathode may cause

agglomeration, and thus block the reaction sites, and discontinue the transport path of oxide ions and protons which, in turn, hinders the reduction reaction.
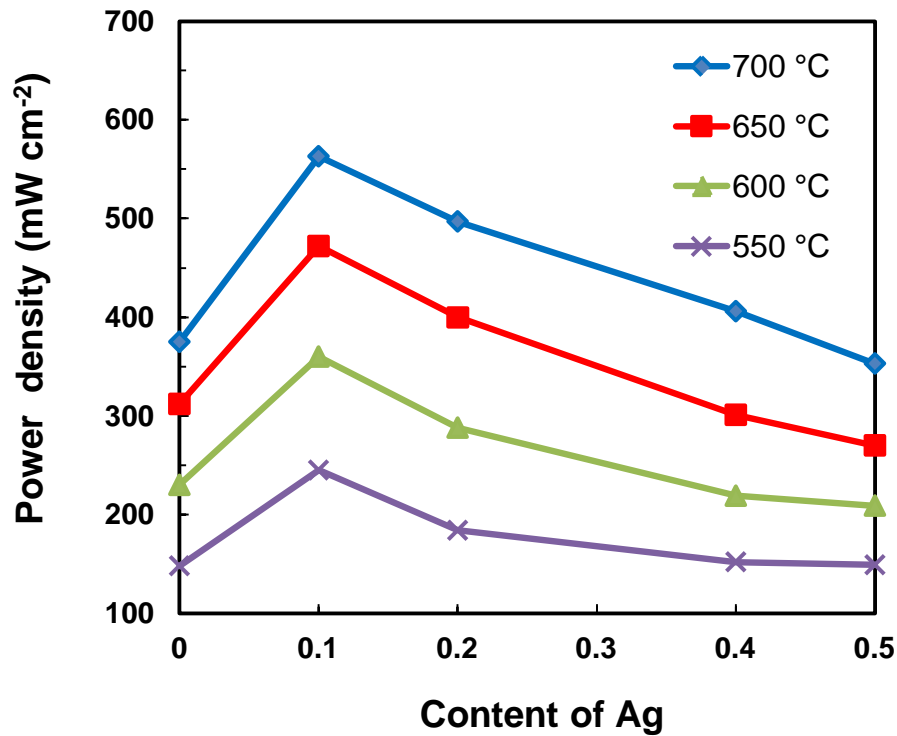
Figure 4.16. Peak power density for single cells as a function of Ag content in cathode catalyst.

Shown in Figure 4.17 is the EIS of thin film single cells with different amount of Ag tested at 600 °C under OCV conditions. Both the ohmic resistance and polarization resistance of the button cell was decreased with 10 wt% Ag, because the addition of Ag increased the electronic conductivity and electro-catalytic activity of ceramic oxide LSCF. Interestingly, for the single cells with greater Ag addition, both the ohmic loss and polarization increased

with an increase of Ag content in accordance with the performances compared in Figure 4.17.
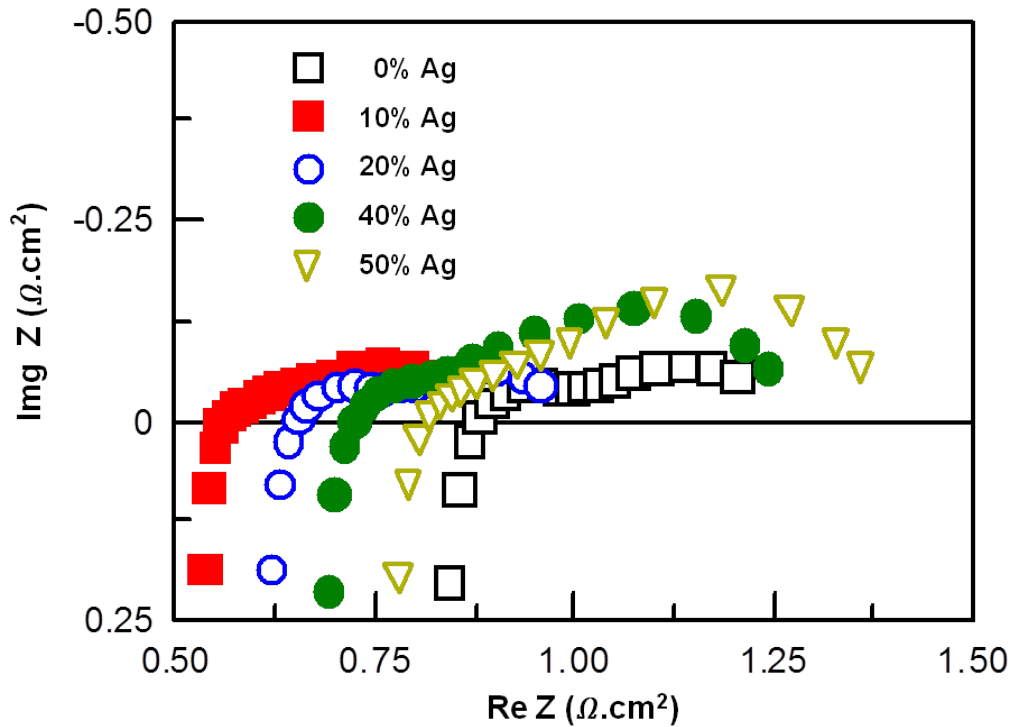
Figure 4.17. EIS of the single cell with different Ag content in the cathode, at 600 °C under OCV conditions in Nyquist plot.

Figure 4.18 shows the *I-V* curves of a typical cell with 10 wt% Ag cathode operating on H_2 fuel at temperatures between 550 and 700 °C. The OCVs were 1.16, 1.13, 1.10 and 1.06V at 550, 600, 650 and 700 °C, respectively, which were higher than those of other reported thin film protonic SOFCs *(16, 17, 92, 93)*. This indicated that the electrolyte was dense enough to prevent gas crossover. The linear correlation between the voltage and applied

current shows that concentration polarization did not take place, even at high current density. This further proves that the composite cathode was porous enough for the gaseous oxygen passing through and the addition of 10 wt% Ag did not cause agglomeration problems at the cathode. The peak power densities at 550, 600, 650, 700 °C were very promising: 245, 360, 472, and 563 mW.cm^{-2}, respectively.
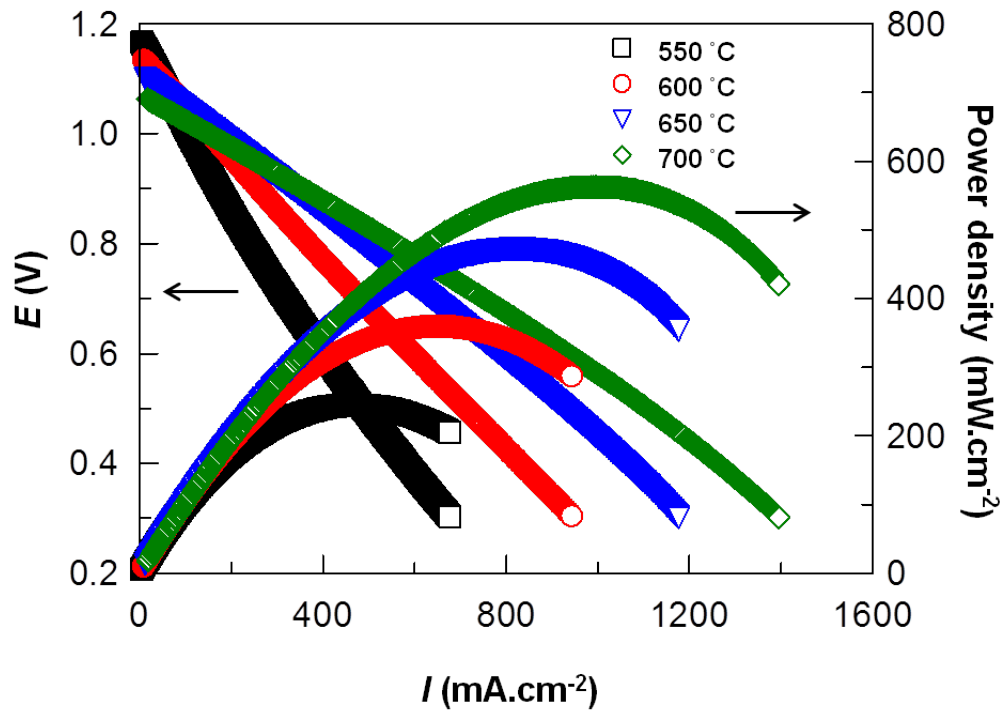
Figure 4.18. *I-V* and power density curves of the Ni+BCZY|BCZY|10 wt% Ag-(LSCF+BCZY) single cells with H$_2$ as the fuel at various temperatures.

To get more information, the impedance spectra of the cell with 10 wt% Ag at various temperatures under OCV conditions were collected as Nyquist

plots shown in Figure 4.19 (a). Ohmic resistance (R_{ohm}) is indicated by the intercept at high frequency with the real axis while polarization resistance (R_p) is given by the intercept of the impedance plot between high frequency and low frequency with the real axis and is related to the electrochemical reactions at both cathode/electrolyte and anode/electrolyte interfaces. The resistances decreased dramatically with increase in temperature. Figure 4.19 (b) shows the calculated resistances (R_{ohm}, R_p and R_{total}) obtained from EIS in Figure 4.19 (a). A very low area specific polarization resistance of 0.07 $\Omega.cm^2$ was obtained at 700 °C which resulted in the high performance. R_{ohm} increased from 0.40 $\Omega.cm^2$ at 700 °C to 0.71 $\Omega.cm^2$ at 550 °C while R_p increased from 0.07 $\Omega.cm^2$ at 700 °C to 1.04 $\Omega.cm^2$ at 550 °C. When the temperature decreased from 700 °C to 550 °C, R_{ohm} almost doubled while R_p increased by 14 times which confirmed that polarization resistance was the predominant factor in the total cell resistance for the cell performance.
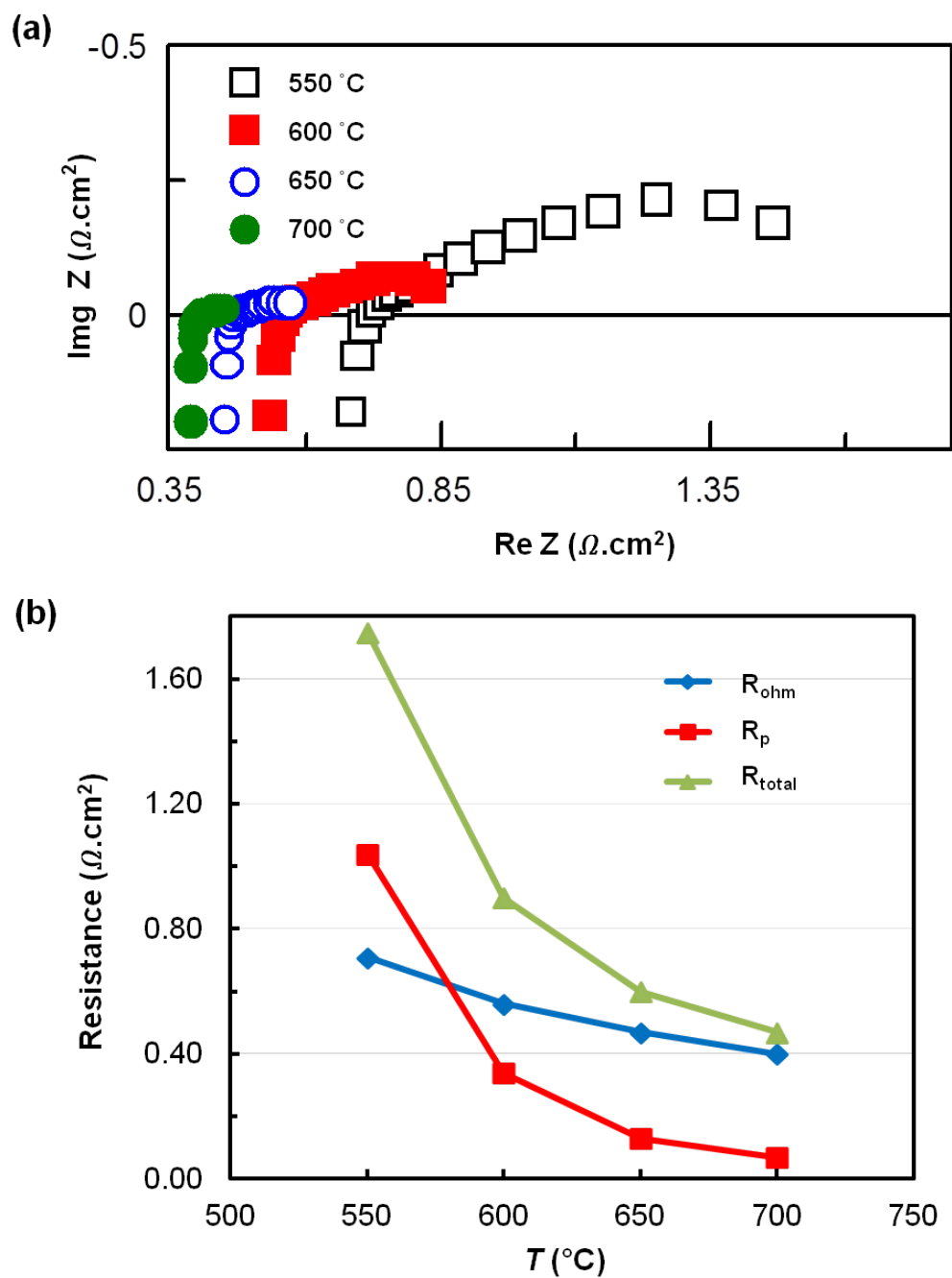
Figure 4.19. (a) Impedance spectra of the single cells with 10 wt% Ag tested under OCV, and (b) calculated resistances of the tested cell as a function of temperature.

It is critical to evaluate the long term durability of the single cell with a 10 wt% Ag-(LSCF+BCZY) composite cathode. One potential problem with Ag modified SOFC is that an operating temperature close to its melting point may cause agglomeration of Ag and thus deterioration of the cell performance with time. The stability test under cell operating condition was conducted at a constant applied potential of 0.75 V at 700 °C and the response current density is shown in Figure 4.20. The current density was relatively stable and there was no substantial degradation in the cell performance within three days operation, indicating that the composite cathode was a stable candidate material for practical application in protonic SOFCs at 700 °C and lower temperatures.
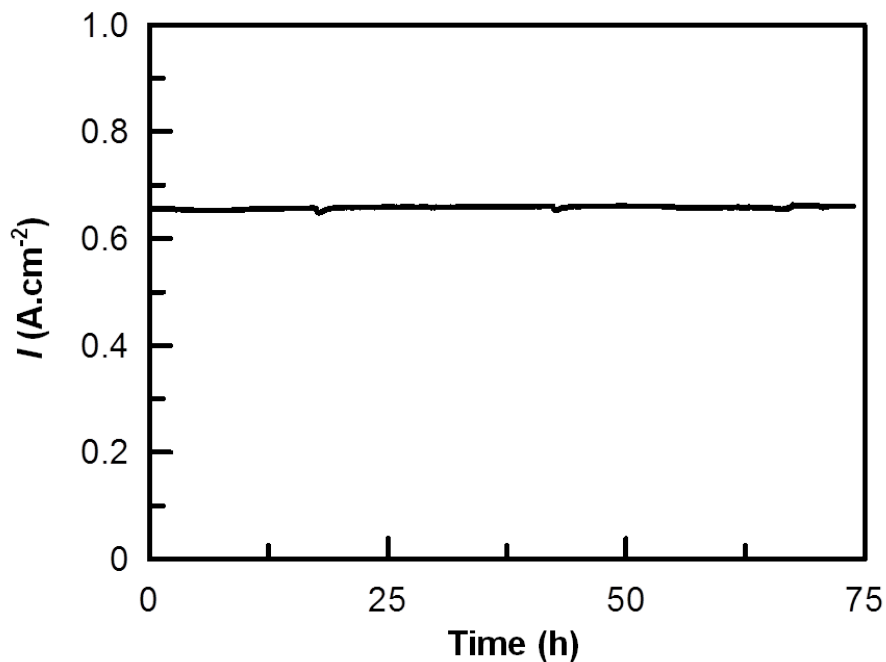
Figure 4.20. Long-term stability of the Ni+BCZY|BCZY|10 wt% Ag-(LSCF+BCZY) single cell at a constant output voltage of 0.75 V at 700 °C.

4.3.5 Summary of Testing of Ag-(LSCF+BCZY) as Cathode Catalyst

Cathode material LSCF was prepared using a citrate-nitrate combustion method. LSCF was stable against a CO_2-containing atmosphere and chemically compatible with electrolyte material BCZY at temperatures up to 1000 °C. The admixed composite cathode with Ag demonstrated improved catalytic activity toward oxygen reduction reaction compared to a LSCF+BCZY cathode without Ag. A long term durability test showed the composite cathode was stable.

4.4 $Sr_{0.7}Ce_{0.3}MnO_{3-\delta}$ as Cathode Catalyst

4.4.1 Introduction

While a composite cathode was used to improve the performance of a known cathode catalyst for protonic SOFCs, as described in the previous section, the development of alternative materials was a parallel research focus.

SCM has been studied as a cathode material for oxygen conducting SOFCs. It is a mixed ionic and electronic conductor with a total conductivity as high as 200-300 $S.cm^{-2}$ in the temperature range 500-700 °C *(94-96)*. The thermal expansion coefficient of SCM ($\sim 11.8*10^{-6}$ K^{-1}) *(96)* is close to that of the electrolyte $BaCeO_3$ ($11.2*10^{-6}$ K^{-1}) *(69)*.

As SCM is a novel material that was first employed in protonic SOFCs, in order to study its performance, SCM was used directly as the cathode and a composite cathode with SCM and BCZY was not investigated at this time.

4.4.2 Characterization of SCM

SCM was prepared using the citrate-nitrate combustion method and the ratio of the total metal ions: citric acid: NH_4NO_3 was set to be 1:1.5:3.5. As shown in Figure 4.21, the pure phase SCM was obtained after calcining the as-prepared powder at 1300 °C for 5 h.
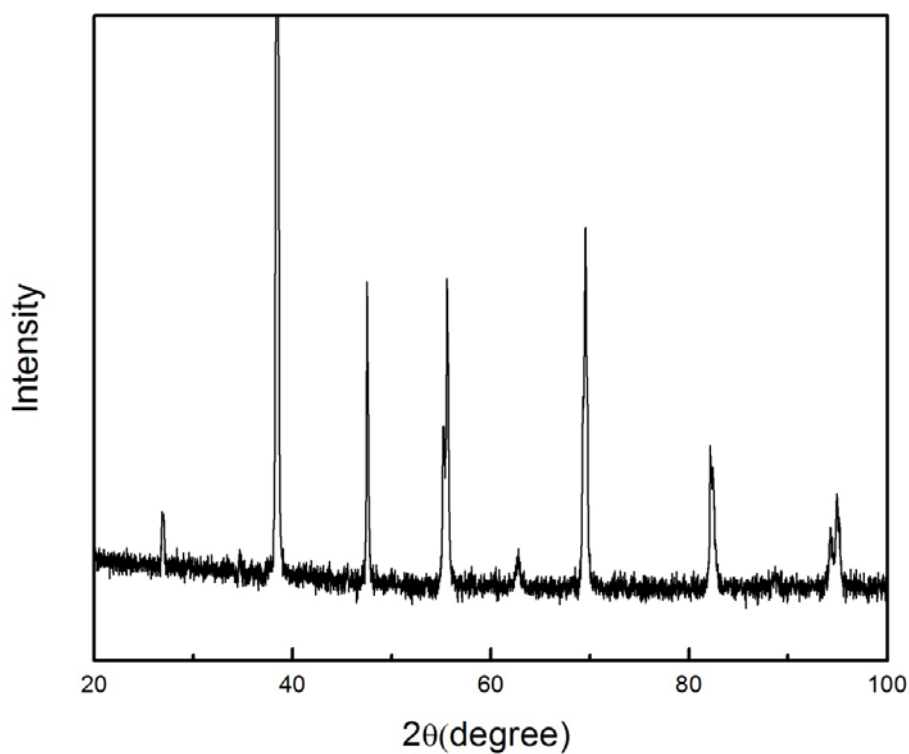
Figure 4.21. XRD pattern of SCM calcined at 1300 °C for 5 h.

4.4.3 Fabrication of the Anode Supported Single Cells

To prepare a SCM cathode on the anode supported electrolyte, slurry with SCM and vehicle ink was brush painted onto the BCZY electrolyte surface

and then fired at different temperatures for 3 h. The brushed cathode should be fired at a sufficiently high temperature to ensure good adhesion of the SCM cathode layer to the electrolyte layer. However, the firing temperature also should be sufficiently low to minimize any phase reaction between cathode and electrolyte materials during the fabrication. In this study, the firing temperatures 1000, 1100 and 1200 °C were compared. Shown in Figure 4.22 are the SEM images of the cathodes fired at different temperatures after running the single cells. Grain sizes of SCM cathodes increased with an increase in firing temperature, which was ascribable to sintering. The cathode and electrolyte layers were well attached to each other after firing at 1100 (Figure 4.22 (b)) and 1200 °C (Figure 4.22 (c)), and the grains of the porous structure were around 2 μm and well connected with necks which ensured the transport of electrons and oxide ions. The cell fired at 1000 °C (Figure 4.22(a)) had good adhesion between electrode and electrolyte and the grains were finer than the other two; however, there were no obvious grain necks between particles.
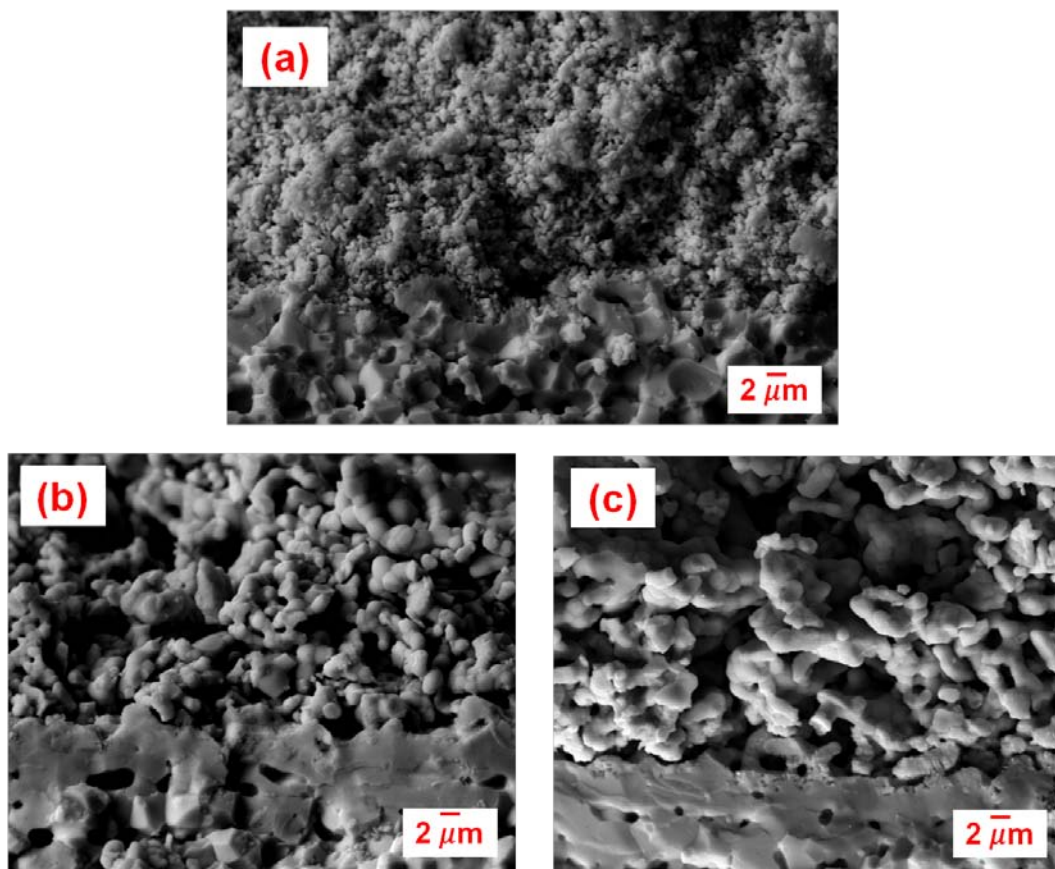
Figure 4.22. SEM images for SCM cathode fired at (a) 1000 °C, (b) 1100 °C, and (c) 1200 °C after single cell test.

4.4.4 Electrochemical Performance of Single Cells

The electrochemical performances of the cells based on a thin film BCZY electrolyte and SCM cathodes fired at 1000, 1100, and 1200 °C were compared under various fuel cell operating conditions. Shown in Figure 4.23 are the current-voltage characteristics and the corresponding power densities for Ni+BCZY|BCZY|SCM single cells with a SCM cathode fired at 1100 °C. The OCVs at 700, 650, 600 and 550 °C were 1.06, 1.10, 1.13 and 1.15V,

respectively, indicating that the BCZY electrolyte was sufficiently dense and exhibited negligible electron and fuel crossover. The peak power densities were about 378, 254, 205 and 124 mW.cm^{-2} at 700, 650, 600 and 550 °C, respectively.

The observed fuel cell performances are very encouraging, especially for operation at low temperatures. In comparison, peak densities for anode supported proton conducting SOFC with LSCF as cathode catalyst were reported to be 235 and 81 mW.cm^{-2} at 650 and 550 °C *(17)* which were slightly lower than the 254 and 124 mW.cm^{-2} observed in this study.
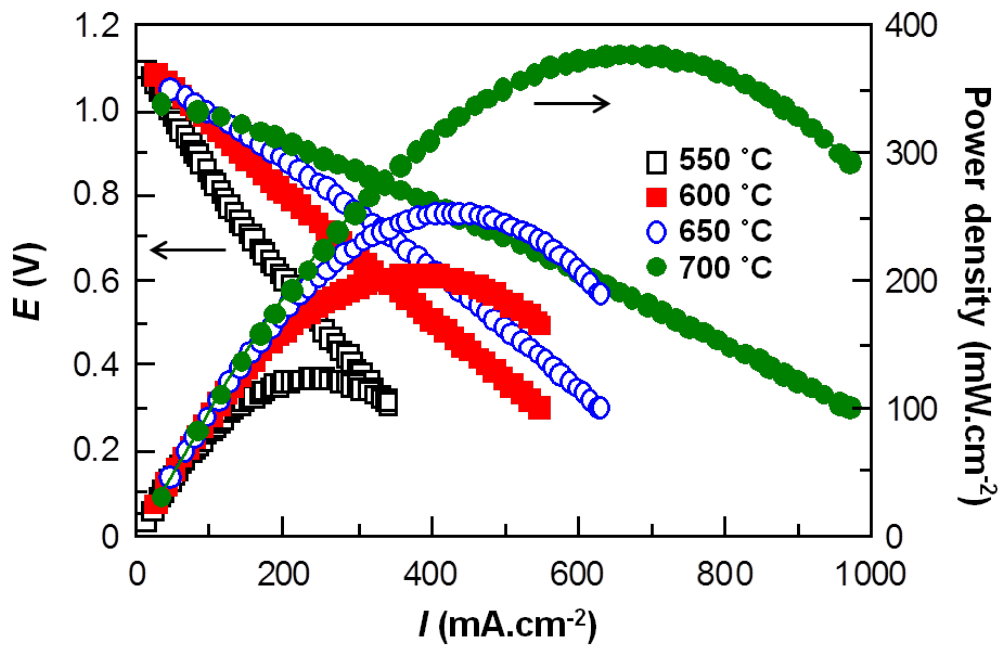
Figure 4.23. *I-V* and power density curves of the Ni+BCZY|BCZY|SCM single cells with SCM cathode fired at 1100 °C.

Shown in Figure 4.24 are the current densities measured at a cell voltage of 0.7 V at various temperatures for cells with SCM cathodes fired at 1000, 1100 and 1200 °C. The button cell with a cathode fired at 1100 °C displayed the highest current densities, 0.50, 0.34, 0.27 and 0.16 A.cm^{-2} at 700, 650, 600 and 550 °C. For the cell with a SCM cathode fired at 1000 °C, the current densities of the cell were reduced to about 0.38, 0.26, 0.18 and 0.10 A.cm^{-2} at 700, 650, 600 and 550 °C, respectively which may be due to insufficient connections between cathode grains. Similarly, when the cathode was fired at 1200 °C, the peak power density dropped to 0.30, 0.19, 0.11 and 0.06 A.cm^{-2} at 700, 650, 600 and 550 °C, respectively, which may result from reactions between electrolyte BCZY and cathode SCM during high temperature firing.
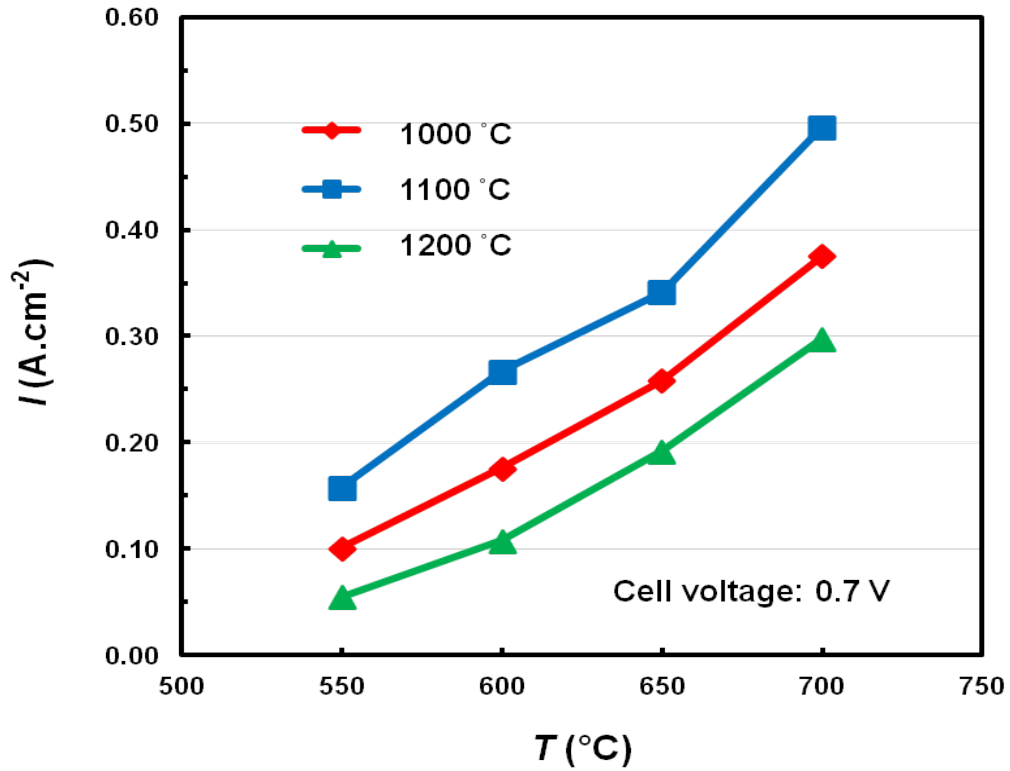
Figure 4.24. Current densities measured at a cell voltage of 0.7 V at different temperatures for the cells with SCM cathode fired at 1000, 1100 and 1200 °C.

Shown in Figure 4.25 are the polarization resistances of the single cells with SCM cathodes fired at 1000, 1100 and 1200 °C. These polarization resistances were determined from impedance spectroscopy under OCV conditions. In accordance with the performance, as expected, the cell with a SCM cathode fired at 1100 °C showed the lowest interfacial resistance and total resistance. At 700 and 650 °C, the interfacial resistances were estimated to be about 0.11 and 0.26 $\Omega.cm^2$, respectively, comparable to the interfacial resistance of the LSCF cathode on the BCZY electrolyte *(17)*. Both the

polarization resistance and total resistance were close for the SCM fired at 1000 and 1200 °C.
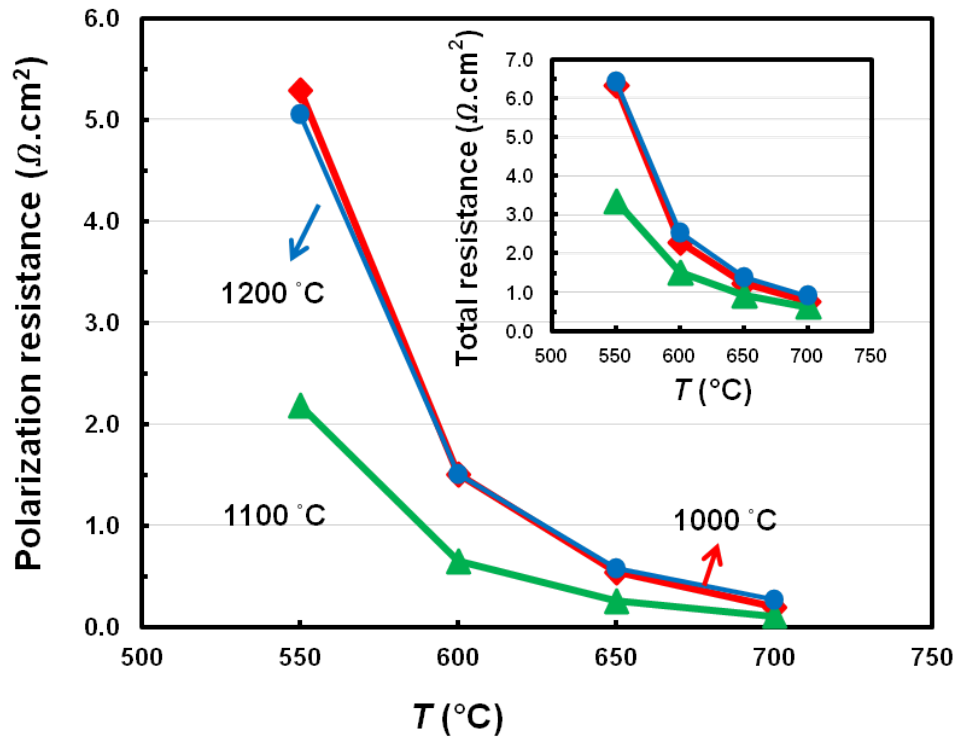
Figure 4.25. Polarization resistances of the single cells with cathodes fired at different temperatures under OCV conditions. The embedded figure depicts the total resistances.

4.4.5 Summary of Testing of SCM as Cathode Catalyst

SCM cathode material was prepared using the citrate-nitrate combustion method at 1300 °C for 5 h. A promising peak power density of 378 mW.cm^{-2} was observed at 700 °C with a cathode fired at 1100 °C. Cathode firing

temperature affected the electrochemical performance as it affected the microstructure of the cathode and the best firing temperature for SCM was 1100 ℃.

Chapter 5   Conclusions and Future Work

Protonic SOFCs can be operated at intermediate temperature due to the relatively low activation energy for proton transport through the electrolyte. However, their performance is still not as high as that of oxide ion conducting SOFCs. Ohmic resistance and cathodic polarization resistance are the two important factors limiting the performance. In this project, improving the electrolyte ohmic loss and cathodic polarization was the study's focus.

5.1 Electrolyte Preparation

The electrolyte BCZY, prepared using a citrate-nitrate combustion method, has a good combination of chemical stability against CO_2, sinterability and conductivity. BCZY powders were stable in CO_2-containing atmospheres. Pellets with density about 95% of theoretical were obtained by sintering green disks at 1500 °C for 10 h. These BCZY membranes had good conductivity in humidified 10% H_2/He: 11, 20 and 33 mS.cm^{-1} at 550, 650 and 750 °C, respectively.

Thin film dense layers of electrolyte were prepared using a spin coating method. The thickness was controlled by changing the number of coatings applied. SEM and OCV of the single cells showed that about 40 μm thick dense electrolyte layers were obtained using six coatings after firing at 1400 °C.

It is possible to further decrease the thickness of electrolyte below 40 μm by reducing coating times and changing the recipe of the slurry. When the

spin coating slurry is less viscous it forms a thinner layer with each coating and thus thinner electrolyte membranes with the same number of coatings. However, as the slurry preparation is a time-consuming trial and error process and the result obtained was applicable, this project did not go into further detail to achieve the best results.

5.2 Ag-modified LSCF+BCZY as Cathode Catalyst

Ag-modified composite cathodes with different Ag content were prepared and tested in an anode supported protonic SOFC. While Ag improves the performance of cathode catalyst with synergetic effect with ceramic oxide and high electronic conductivity, addition Ag retards the reaction as Ag particles are dispersed on the surface of LSCF and BCZY which block the reaction surface. The effect on the performance of cathode catalyst depends on this twoe factor. Addition of a low amount of Ag decreased the ohmic resistances and thus improved the performance, but higher amount of Ag in the cathode were less effective. Cathodes with 10 wt% Ag content had the best performance. A high power density of 563 $mW.cm^{-2}$ was achieved at 700 °C for button cells with a 10% Ag cathode. Long term stability tests showed that the cathode was stable under operating conditions.

Herein, a mechanical admix of Ag and LSCF+BCZY was used to evaluate the effect of Ag on the performance of the cathode. Better results may be achieved by optimizing the cathode microstructure and the Ag and LSCF content using an impregnation method. A preliminary experiment was

conducted to impregnate LSCF into the porous backbone of BCZY. Figure 5.1 shows the SEM image of the impregnated structure. Nano-particulate LSCF fully covered the porous BCZY backbone with grains connected by necks, which ensures the transport path of both oxide ions and electrons.
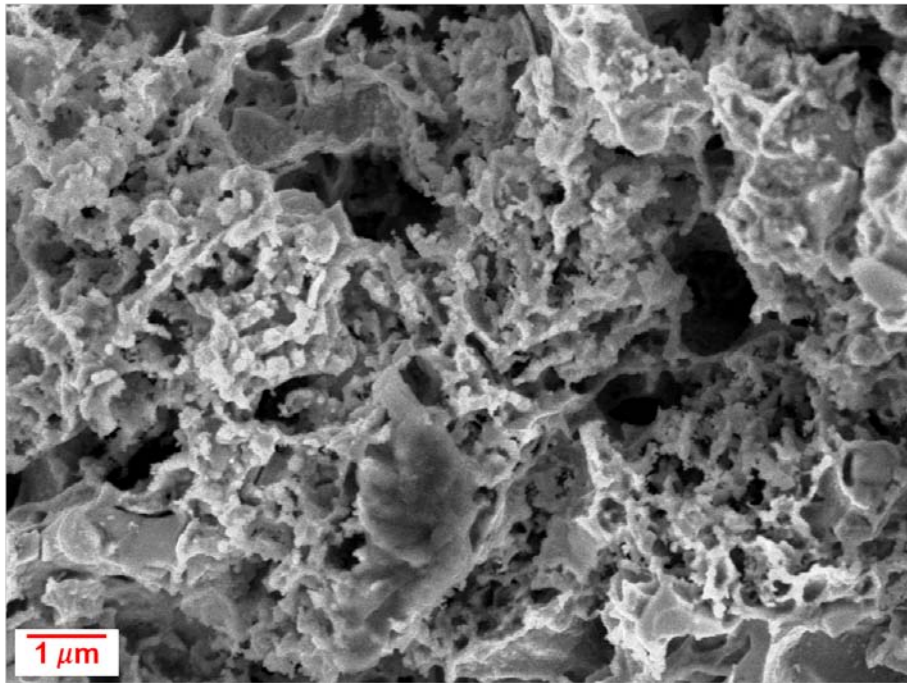
Figure 5.1. SEM image of LSCF impregnated into the BCZY porous structure.

5.3 SCM as Cathode Catalyst

SCM was successfully synthesized and employed in the proton conducting SOFC. The effect of firing temperature on the cathode was investigated by determining the respective microstructures and the electrochemical performance in a full cell. Grain size of the cathode SCM

increased with increase in firing temperature. Grains were connected by necks in SCM cathodes fired at 1100 and 1200 °C. Button cells with cathodes fired at 1100 °C had the best performance, and a peak power density of 378 mW.cm^{-2} was obtained at 700 °C. Both the polarization resistance and ohmic resistance were similar for the cathodes fired 1100 and 1200 °C. In cathodes fired at 1000 °C, there was relatively poor bonding between cathode and electrolyte, with the consequence that the transport paths for both electrons and ions in the cathode had higher resistance, which resulted in poor performance. For cathodes fired at 1200 °C, poor performance is tentatively attributed to the possible reaction between electrolyte and cathode.

Further research is required to more fully investigate chemical stability of the oxides herein in humid atmosphere, and the chemical and thermal compatibility between electrolyte and cathode. Improvement of cathode performance may be achieved through admixture with a protonic conductor and optimization of microstructure.

For the two series of cathode materials developed herein, the mechanism of the oxygen reduction reaction and optimization of anode substrate and functional layer are not yet fully elucidated, and so may be the subjects for future work to enable rational improvements in materials and process design.

Chapter 6   References

1. Energy Information Administration, Department of Energy, *International Energy Outlook 2011*. (Washington, D.C, 2011).

2. IPCC Fourth Assessment Report Synthesis Report: Summary for Policymakers. (2007).

3. R. O'Hayre, S.-W. Cha, W. Colella, F. B. Prinz, *Fuel Cell Fundamentals*. (John Wiley & Sons, Inc., Hoboken, New Jersey, 2006).

4. EG&G Services Parsons, Inc., Science Applications International Corporation, *Fuel Cell Handbook*. (Morgantown, West Virginia, ed. Fifth, 2000).

5. A. Bauen, D. Hart, *Journal of Power Sources* **86**, 482 (2000).

6. B.C.H. Steele, A. Heinzel, *Nature* **414**, 345 (2001).

7. A. Vincent, J.-L. Luo, K.T. Chuang, A.R. Sanger, *Journal of Power Sources* **195**, 769 (2010).

8. C.M. Grgicak, J.B. Giorgi, *The Journal of Physical Chemistry C* **111**, 15446 (2007).

9. C.M. Grgicak, R.G. Green, J.B. Giorgi, *Journal of Power Sources* **179**, 317 (2008).

10. C.M. Grgicak, M.M. Pakulska, J.S. O'brien, J.B. Giorgi, *Journal of Power Sources* **183**, 26 (2008).

11. Z. Shi, J.-L Luo, S. Wang, A.R. Sanger, K.T. Chuang, *Journal of Power Sources* **176**, 122 (2008).

12. C. Zuo, S. Zha, M. Liu, M. Hatano, M. Uchiyama, *Advanced Materials* **18**, 3318 (2006).

13. S. Tao, J.T.S. Irvine, *Advanced Materials* **18**, 1581 (2006).

14. R. Haugsrud, T. Norby, *Nature Materials* **5**, 193 (2006).

15. K.D. Kreuer, *Annual Review of Materials Research* **33**, 333 (2003).

16. L. Yang, C. Zuo, S. Wang, Z. Cheng, M. Liu, *Advanced Materials* **20**, 3280 (2008).

17. L. Yang, Z. Lei, S. Wang, Y. Choi, C. Zuo, M. Liu, *Journal of Power Sources* **195**, 471 (2010).

18. D.R. Gaskell, *Introduction to Thermodynamics of Materials*, (Taylor & Francis, New York, ed. Fifth, 2008).

19. D. Chen, R. Ran, K. Zhang, J. Wang, Z. Shao, *Journal of Power Sources* **188**, 96 (2009).

20. F.A. Kröger, H.J. Vink, *Solid State Physics* **3**, 307 (1956).

21. A.J. Jacobson, *Chemistry of Materials* **22**, 660 (2010).

22. R. Peng, T. Wu, W. Liu, X. Liu, G. Meng, *Journal of Materials Chemistry* **20**, 6218 (2010).

23. B.A. Boukamp, *Nature Materials* **2**, 294 (2003).

24. S.P. Jiang, J. Li, in *Solid Oxide Fuel Cells: Materials Properties and Performance* J.W. Fergus, R. Hui, X. Li, D.P. Wilkinson, J. Zhang, Eds. (CRC Press, Boca Raton, 2009).

25. S P. Jiang, *Solid State Ionics* **146**, 1 (2002).

26. J. Mizusaki, Y. Yonemura, H, Kamata, K. Ohyama, N. Mori, H. Takai, H. Tagawa, M. Dokiya, K. Nayara, T. Sasamoto, H. Inaba, T. Hashimoto, *Solid State Ionics* **132**, 167 (2000).

27. A. Endo, M. Ihara, H. Komiyama, K. Yamada, *Solid State Ionics* **86-88**, 1191 (1996).

28. S.T. Aruna, M. Muthuraman, K.C. Patil, *Journal of Materials Chemistry* **7**, 2499 (1997).

29. S. Carter, A. Selcuk, R.J. Chater, J. Kajda, J.A. Kilner, B.C.H. Steele, *Solid State Ionics* **53-56**, 597 (1992).

30. I. Yasuda, K. Ogasawara, M. Hishinuma, T. Kawada, M. Dokiya, *Solid State Ionics* **86-88**, 1197 (1996).

31. S.P. Jiang, J.P. Zhang, K. Fogerb, *Journal of The Electrochemical Society* **147**, 3195 (2000).

32. E.P. Murray, T. Tsai, S.A. Barnett, *Solid state ionics* **110**, 235 (1998).

33. E.P. Murray, S.A. Barnett, *Solid State Ionics* **143**, 265 (2001).

34. S.P. Jiang, W. Wang, *Journal of The Electrochemical Society* **152**, A1398 (2005).

35. S.P. Jiang, W. Wang, *Solid State Ionics* **176**, 1351 (2005).

36. P. Plonczak, M. Gazda, B. Kusz, P. Jasinski, *Journal of Power Sources* **181**, 1 (2008).

37. A. Mai, V.A.C. Haanappel, S. Uhlenbruck, F. Tietz, Dö Str, *Solid State Ionics* **176**, 1341 (2005).

38. S.P. Simner, M.D. Anderson, L.R. Pederson, J.W. Stevenson, *Journal of The Electrochemical Society* **152**, A1851 (2005).

39. G.W. Coffey, J. Hardy, L.R. Pedersen, P.C. Rieke, E.C. Thomsen, M. Walpole, *Solid State Ionics* **158**, 1 (2003).

40. G.W. Coffey, J.S. Hardy, L.R. Pederson, P.C. Rieke, E.C. Thomsen, *Electrochemical and Solid-State Letters* **6**, A121 (2003).

41. A.N. Petrov, O.F. Kononchuk, A.V. Andreev, V.A. Cherepanov, P. Kofstad, *Solid State Ionics* **80**, 189 (1995).

42. A. Petric, P. Huang, F. Tietz, *Solid State Ionics* **135**, 719 (2000).

43. Y. Teraoka, T. Nobunaga, K. Okamoto, N. Miura, N. Yamazoe, *Solid State Ionics* **48**, 207 (1991).

44. W. Zhou, R. Ran, Z. Shao, *Journal of Power Sources* **192**, 231 (2009).

45. Y. Teraoka, H.M. Zhang, K. Okamoto, N. Yamazoe, *Materials Research Bulletin.* **23**, 51 (1988).

46. Y. Teraoka, H.M. Zhang, S. Furukawa, N. Yamzoe, *Chemistry Letters*, 1743 (1985).

47. Y. Matsumoto, S. Yamada, T. Nishida, E. Sato, *Journal of Electrochemical Society* **127**, 2360 (1980).

48. V.V. Kharton, A.A. Yaremchenko, A.L. Shaula, M.V. Patrakeev, E.N. Naumovich, D.I. Logvinovich, J.R. Frade, F.M.B. Marques, *Journal of Solid State Chemistry* **177**, 26 (2004).

49. A.A. Yaremchenko, V.V. Kharton, M.V. Patrakeev, J.R. Frade, *Journal of Materials Chemistry* **13**, 1136 (2003).

50.   J.M. Bassat, P. Odier, A. Villesuzanne, C. Marin, M. Pouchard, *Solid State Ionics* **167**, 341 (2004).

51.   S.J. Skinner, J.A. Kilner, *Solid State Ionics* **135**, 709 (2000).

52.   D. Huang, Q Xu, F. Zhang, W. Chen, H. Liu, J. Zhou, *Materials Letters* **60**, 1892 (2006).

53.   C.N. Munnings, S.J. Skinner, G. Amow, P.S. Whitfield, I.J. Davidson, *Solid State Ionics* **176**, 1895 (2005).

54.   A. Aguadero, M.J. Escudero, M. P*érez, Dalton Transactions*, 4377 (2006).

56.   K. Zhang, L. Ge, R. Ran, Z. Shao, S. Liu, *Acta Materialia* **56**, 4876 (2008).

57.   A. Tarancón, A. Morata, G. Dezanneau, S.J. Skinner, J.A. Kilner, S Estradé, F. Hernández-Ramírez, F. Peiró, J.R. Morante, *Journal of Power Sources* **174**, 255 (2007).

58.   H. Ding, X. Xue, *International Journal of Hydrogen Energy* **35**, 2486 (2010).

59.   J.H. Kim, F. Prado, A. Manthiram, *Journal of The Electrochemical Society* **155**, B1023 (2008).

60.   J.H. Kim, M. Cassidy, J.T.S. Irvine, J. Bae, *Journal of The Electrochemical Society* **156**, B682 (2009).

61.   G. Kim, S. Wang, A.J. Jacobson, L. Reimus, P. Brodersen, C.A. Mims *Journal of Materials Chemistry* **17**, 2500 (2007).

62. J.H. Kim, A. Manthiram, *Journal of The Electrochemical Society* **155**, B385 (2008).

63. Y. Lin, R. Ran, C. Zhang, R. Cai, Z. Shao, *Journal of Physical Chemistry A* **114**, 3764 (2010).

64. Z. Tao, L. Bei, L. Yan, W. Sun, Z. Zhu, R. Peng, W. Liu, *Electrochemistry Communications* 688 (2009).

65. Z. Tao, L. Bi, Z. Zhu, W. Liu, *Journal of Power Sources* **194**, 801 (2009).

66. X.-Z. Fu, J.-L. Luo, A.R. Sanger, N. Danilovic, K.T. Chuang, *Chemical Communications* **46**, 2052 (2010).

67. T. Takahashi, H. Iwahara, *Revue de Chimie Minerale* **17**, 11 (1980).

68. K.H. Ryu, S.M. Haile, S*olid State Ionics* **125**, 355 (1999).

69. S. Yamanaka, M. Fujikane, T. Hamaguchi, H. Muta, T.Matsuda S. Kobayashi, K. Kurosaki, *Journal of Alloys and Compounds* **359**, 109 (2003).

70. E. Fabbri, A. D'Epifanio, E.D. Bartolomeo, S. Licoccia, E. Traversa, *Solid State Ionics* **179**, 558 (2008).

71. H. Iwahara, *solid State Ionics* **77**, 289 (1995).

72. W. Suksamai, I.S. Metcalfe, *Solid State Ionics* **178**, 627 (2007).

73. N. Bonanos, *Solid State Ionics* **53-56**, 967 (1992).

74. G. Chiodelli, L. Malavasi, C.Tealdi, S. Barison, M, Battagliarin, L. Doubova, M. Fabrizio, C. Mortalò, R. Gerbasi, *Journal of Alloys and Compounds* **470**, 477 (2009).

75.   H. Iwahara, *Solid State Ionics* **86-88**, 9 (1996).

76.   T. Norby, Y. Larring, *Current Opinion in Solid State and Materials Science* **2**, 593 (1997).

77.   M.J. Scholten, J. Schoonman, J.C. van Miltenburg, H.A.J. Oonk, *Solid State Ionics* **61**, 83 (1993).

78.   K. Katahira, Y. Kohchi, T. Shimura, H. Iwahara, *Solid State Ionics* **138**, 91 (2000).

79.   S. Ricote, N. Bonanos, M.C. Marco de Lucas, G. Caboche, *Journal of Power Sources* **193**, 189 (2009).

80.   W.Z. Zhu, S.C. Deevi, *Materials Science and Engineering A* **A362**, 228 (2003).

81.   N.Q. Minh, *Journal of American Ceramic Society* **76**, 563 (1993).

82.   P.Y. Min, C.G. Man, *Solid State Ionics* **120**, 265 (1999).

83.   S. Wang, T. Kobayashi, M. Dokiya, T. Hashimotob, *Journal of The Electrochemical Society* **147**, 3606 (2000).

84.   K. Kendall, N.Q. Minh, S.C. Singhal, in *High Temperature Solid Oxide Fuel Cells,* S.C. Singhal, K. Kendall, Eds. (Elsevier, 2003).

85.   H. Ding, X. Xue, *Journal of Alloys and Compounds* **496**, 683 (2010).

86.   M. Sahibzada, S.J. Benson, R.A. Rudkin, J.A. Kilner, *Solid State Ionics* **113-115**, 285 (1998).

87.   S.P. Simner, J.F. Bonnett, N.L. Canfield, K.D. Meinhardt, J.P. Shelton, V.L. Sprenkle, J.W. Stevenson, *Journal of Power Sources* **113**, 1 (2003).

88.   S. Wang, T. Kato, S. Nagata, T. Honda, T. Kaneko, N. Iwashita, M. Dokiya, *Solid State Ionics* **146**, 203 (2002).

89.   Y. Liu, M. Mori, Y. Funahashi, Y. Fujishiro, A. Hirano, *Electrochemistry Communications* **9**, 1918 (2007).

90.   L.W. Tai, M.M. Nasrallah, H.U. Anderson, D.M. Sparlin, S.R. Sehlin, *Solid State Ionics* **76**, 273 (1995).

91.   Y. Lin, R. Ran, Z. Shao, *International Journal of Hydrogen Energy* **35**, 8281 (2010).

92.   L. Zhao, B. He, B. Lin, H. Ding, S. Wang, Y. Ling, R. Peng, G. Meng, X. Liu. *Journal of Power Sources* **194**, 835 (2009).

93.   H. Ding, X. Xue, X. Liu, G. Meng, *Journal of Power Sources* **194**, 815 (2009).

94.   A.A. Yaremchenko, A.V. Kovalevsky, V.V. Kharton, *Solid State Ionics* **179**, 2181 (2008).

95.   S. Hashimoto, H. Iwahara, *Materials Research Bulletin* **35**, 2253 (2000).

96.   I.P. Marozau, V.V. Kharton, A.P. Viskup, J.R. Frade, V.V. Samakhval, *Journal of the European Ceramic Society* **26**, 1371 (2006).